



저작자표시-비영리-변경금지 2.0 대한민국

이용자는 아래의 조건을 따르는 경우에 한하여 자유롭게

- 이 저작물을 복제, 배포, 전송, 전시, 공연 및 방송할 수 있습니다.

다음과 같은 조건을 따라야 합니다:



저작자표시. 귀하는 원저작자를 표시하여야 합니다.



비영리. 귀하는 이 저작물을 영리 목적으로 이용할 수 없습니다.



변경금지. 귀하는 이 저작물을 개작, 변형 또는 가공할 수 없습니다.

- 귀하는, 이 저작물의 재이용이나 배포의 경우, 이 저작물에 적용된 이용허락조건을 명확하게 나타내어야 합니다.
- 저작권자로부터 별도의 허가를 받으면 이러한 조건들은 적용되지 않습니다.

저작권법에 따른 이용자의 권리는 위의 내용에 의하여 영향을 받지 않습니다.

이것은 [이용허락규약\(Legal Code\)](#)을 이해하기 쉽게 요약한 것입니다.

[Disclaimer](#)

Ph.D. DISSERTATION

Towards Autonomous Driving :  
Surrounding Environment Classification  
and DOA Estimation via Advanced Radar  
Signal Processing

자율 주행을 향하여 : 향상된 레이더 신호처리를 통한  
도로 환경 분류 및 도래각 추정

BY

SIM HEONKYO  
FEBRUARY 2020

DEPARTMENT OF ELECTRICAL AND  
COMPUTER ENGINEERING  
COLLEGE OF ENGINEERING  
SEOUL NATIONAL UNIVERSITY

Ph.D. DISSERTATION

Towards Autonomous Driving :  
Surrounding Environment Classification  
and DOA Estimation via Advanced Radar  
Signal Processing

자율 주행을 향하여 : 향상된 레이더 신호처리를 통한  
도로 환경 분류 및 도래각 추정

BY

SIM HEONKYO  
FEBRUARY 2020

DEPARTMENT OF ELECTRICAL AND  
COMPUTER ENGINEERING  
COLLEGE OF ENGINEERING  
SEOUL NATIONAL UNIVERSITY

# Towards Autonomous Driving : Surrounding Environment Classification and DOA Estimation via Advanced Radar Signal Processing

자율 주행을 향하여 : 향상된 레이더 신호처리를 통한  
도로 환경 분류 및 도래각 추정

지도교수 김 성 철  
이 논문을 공학박사 학위논문으로 제출함

2020년 2월

서울대학교 대학원

전기·정보 공학부

심 헌 교

심헌교의 공학박사 학위 논문을 인준함

2020년 2월

위 원 장:	김 남 수	(인)
부위원장:	김 성 철	(인)
위 원:	심 병 효	(인)
위 원:	김 영 록	(인)
위 원:	김 용 화	(인)

# Abstract

Recently, as interest in autonomous driving has increased, research on sensors used for autonomous driving is being actively conducted. These sensors used include cameras, lidars, radars, and ultrasonic devices. Among them, radars have a long maximum detectable range and are robust to harsh environments such as rain or no light. Thus, they are essential sensors for autonomous driving. Radars can be used for various purposes, mainly for adaptive cruise control (ACC) and automatic emergency braking (AEB). They can be used to detect the distance to the target, relative velocity, angle, etc., and they can also detect target type and size.

In this dissertation, I proposed a neural network structure for classifying road environments. Various road environments are encountered in autonomous driving, and applying an appropriate target detection algorithm depending on the road environment is necessary. For example, in an iron tunnel comprising several iron structures, the reflection signal is very strong, causing the target to be undetected. Therefore, to detect a desired target, a clutter removal algorithm should be required. To recognize and classify the road environment from a distance in advance, I proposed a neural network structure. As a result, the accuracy of classifying road environments was improved by approximately 14%p.

In addition, I proposed a method to improve the angular resolution by using an automotive radar. To know the position of the target, the direction-of-arrival (DOA) as well as distance and velocity are essential information. This can be solved by increasing the antenna aperture size; however, increasing the aperture size reduces the field of view and requires considerable space. To solve this problem, I proposed a method for generating virtual received signals using the linearly predicted array expansion. By applying the generated virtual and actual signals to the DOA estimation algorithm, a method of improving the angular resolution using a small antenna aperture size was

proposed. As a result, the proposed method improved the angular resolution by approximately  $3^\circ$ .

Finally, I proposed a technique to distinguish the transmission signal in the multi-input and multi-output (MIMO) radar to improve the DOA estimation performance. If multiple transmitting antennas are used, the targets can be efficiently detected by using a small number of antennas. However, if the signals radiated from each transmit antenna element cannot be distinguished, the DOA estimation performance degrades. To address this problem, I proposed a method to distinguish transmission signals by using a maximum likelihood estimation method. Thus, the maximum detectable velocity was doubled. In addition, the DOA estimation performance was also enhanced by approximately  $3^\circ$  in terms of root mean square error (RMSE).

**keywords:** Automotive radar, deep learning, direction-of-arrival, MIMO radar, road environment classification, road environment recognition, virtual array.

**student number:** 2014-21629

# Contents

<b>Abstract</b>	<b>i</b>
<b>Contents</b>	<b>iii</b>
<b>List of Tables</b>	<b>v</b>
<b>List of Figures</b>	<b>vi</b>
<b>1 INTRODUCTION</b>	<b>1</b>
<b>2 Road structure classification through artificial neural network for automotive radar systems</b>	<b>4</b>
2.1 Introduction . . . . .	4
2.2 System model and target detection in automotive FMCW radar . . . .	6
2.2.1 Fundamental of slow-chirp FMCW radar . . . . .	6
2.2.2 Sensor parameter description . . . . .	7
2.2.3 Target detection in various road structures . . . . .	8
2.3 Road structure classification via ANN . . . . .	13
2.4 Target classification results . . . . .	16
2.5 Conclusion . . . . .	24
<b>3 Enhanced DOA Estimation Using Linearly Predicted Array Expansion for Automotive Radar Systems</b>	<b>25</b>

3.1	Introduction . . . . .	25
3.2	DOA Estimation in Array Antenna System . . . . .	28
3.2.1	Signal Model for ULA Antenna . . . . .	28
3.2.2	Bartlett Algorithm . . . . .	29
3.3	Proposed Linearly Predicted Array Expansion . . . . .	30
3.3.1	Forward Linearly Predicted Array Expansion . . . . .	30
3.3.2	Backward Linearly Predicted Array Expansion . . . . .	34
3.4	Simulation Results . . . . .	35
3.5	Experimental Results . . . . .	54
3.6	Computational complexity . . . . .	58
3.7	Conclusion . . . . .	59
<b>4</b>	<b>Improved DOA Estimation Method by Distinction of Different Transmit Signals in Automotive MIMO FMCW Radar Systems</b>	<b>60</b>
4.1	Introduction . . . . .	60
4.2	Fundamentals of fast-ramp FMCW radar system and DML DOA estimation algorithm . . . . .	62
4.2.1	Fundamentals of fast-ramp FMCW radar system . . . . .	62
4.2.2	Coded MIMO radar signal . . . . .	63
4.2.3	Deterministic maximum likelihood . . . . .	64
4.3	Target detection in MIMO radar system . . . . .	66
4.4	Simulation and experiment results . . . . .	71
4.5	Conclusion . . . . .	83
<b>5</b>	<b>Conclusion</b>	<b>84</b>
	<b>Abstract (In Korean)</b>	<b>97</b>

# List of Tables

2.1	Classification performance according to the number of antenna elements.	21
2.2	Confusion matrix when using 3 consecutive scans. . . . .	21
2.3	Classification performance according to the number of scans. . . . .	21
2.4	Confusion matrix when the deep learning is performed using the suggested features in [12]. . . . .	22
2.5	Confusion matrix when the support vector machine with a Gaussian kernel is performed using the suggested features in [12]. . . . .	23
3.1	RMSE and resolution probability of MUSIC DOA estimation methods for two targets . . . . .	53
3.2	RMSE and resolution probability of various DOA estimation methods for three targets . . . . .	55
3.3	RMSE and resolution probability of various DOA estimation methods in actual experiments . . . . .	58
4.1	Values of radar parameters . . . . .	68
4.2	Minimum value of normalized error function according to the antenna array. . . . .	78
4.3	RMSE of true array and false array according to SNR . . . . .	78

# List of Figures

2.1	Snapshots of (a) sound barrier, (b) iron tunnel, (c) typical underground tunnel, and (d) open road. . . . .	10
2.2	Accumulated FFT data for (a) sound barrier, (b) iron tunnel, (c) typical underground tunnel, and (d) open road. . . . .	11
2.3	Instantaneous FFT magnitude responses for: (a) sound barrier, (b) iron tunnel, (c) typical underground tunnel, and (d) open road. . . . .	12
2.4	Framework of the proposed artificial neural network . . . . .	12
2.5	Flowchart of the proposed artificial neural network . . . . .	14
2.6	Classification performance with an increasing number of nodes in the hidden layer when the activation function is: (a) <i>tanh</i> and (b) <i>ReLU</i> . . . . .	17
2.7	Classification performance with an increasing number of hidden layers when the activation function is: (a) <i>tanh</i> and (b) <i>ReLU</i> . . . . .	19
3.1	Linearly predicted expansion (a) forward (b) backward . . . . .	32
3.2	RMSE according to the number of expanded antenna elements (a) without normalization and (b) with normalization . . . . .	38
3.3	Power of the actual (1 to 4) and extrapolated (5 to 16) signals . . . . .	40
3.4	DOA estimation of the Bartlett algorithm with and without the proposed array expansion method for spacing of (a) $0.8\lambda$ and (b) $1.8\lambda$ . . . . .	41

3.5	DOA estimation of the Bartlett algorithm with and without the proposed array expansion method, and it using the conventional LLS method for spacing of (a) $0.8\lambda$ and (b) $1.8\lambda$ . . . . .	42
3.6	DOA estimation of the Bartlett algorithm with and without the proposed array expansion method, and it using conventional extrapolation for spacing of (a) $0.8\lambda$ (b) $1.8\lambda$ . . . . .	44
3.7	RMSE according to the number of antenna elements using the proposed method and conventional extrapolation . . . . .	46
3.8	Resolution probability according to the number of antenna elements using the proposed method and conventional extrapolation . . . . .	46
3.9	RMSE according to the number of targets using the proposed method and conventional extrapolation . . . . .	48
3.10	RMSE according to the number of snapshot using the proposed method and conventional extrapolation . . . . .	48
3.11	RMSE according to SNR using the proposed method and conventional LLS method . . . . .	49
3.12	Resolution probability according to SNR using the proposed method and conventional LLS method . . . . .	49
3.13	Resolution probability according to the DOA difference using the actual array, proposed array, minimum redundancy array, nested array, co-prime array, when SNR is (a) 10dB (b) -5dB . . . . .	51
3.14	Normalized Bartlett pseudospectra of different antenna arrays . . . . .	52
3.15	DOA estimation of the MUSIC algorithm with and without the proposed array expansion method considering correctly estimated ( $\hat{L} = 2$ ) and incorrectly estimated ( $\hat{L} = 3$ ) number of targets . . . . .	53
3.16	Experimental setup with two targets located in front of a radar-equipped vehicle . . . . .	56

3.17	DOA estimation of the conventional Bartlett algorithm with and without the proposed array expansion method, and it using conventional LLS method and conventional extrapolation . . . . .	57
4.1	Transmitted signals from two different transmit antennas . . . . .	64
4.2	MIMO radar system with two transmit antenna elements and four received antenna elements . . . . .	67
4.3	MIMO radar system with true array and false array . . . . .	67
4.4	2D-FFT result when two targets exist in same distance . . . . .	68
4.5	2D-FFT result when two targets exist in different distance . . . . .	70
4.6	Normalized error function of true and false array . . . . .	72
4.7	Normalized pseudospectra of true and false array (a) MUSIC (b) Capon	73
4.8	2D-FFT results when three targets exist . . . . .	74
4.9	DML simulation results of true array and false array for three transmit antenna elements . . . . .	74
4.10	Normalized pseudospectra of true array and false array for three targets (a) MUSIC (b) Capon . . . . .	75
4.11	MIMO radar system with true array and false array with three transmit antennas . . . . .	77
4.12	Normalized error function of true array and false array for three transmit antenna elements . . . . .	77
4.13	Normalized pseudospectra of true and false array for three transmit antenna (a) MUSIC (b) Capon . . . . .	79
4.14	Resolution probability of true array and false array according to SNR	80
4.15	Experimental setup with two targets located in front of a radar-equipped vehicle . . . . .	82
4.16	Normalized error function of true and false array in actual experiment	82
4.17	MUSIC experimental result of true and false array . . . . .	83

# Chapter 1

## INTRODUCTION

Recently, with the rise of autonomous driving as a leader of the fourth industrial revolution, research on radars, which are one of the sensors used in autonomous driving, is being actively conducted [1]. Among the various sensor technologies, radar sensors have become essential because they are robust to harsh weather conditions, compared with cameras and lidar sensors and have a longer detection range than ultrasonic sensors. Further, they are more cost-efficient than lidar sensors [2], [3]. Therefore, studies on automotive radars is being actively conducted for safe autonomous driving on issues [4]–[6] such as target detection [7], [8], target classification [9], and road clutter recognition and suppression [10]–[14].

Automotive radar mainly performs functions such as adaptive cruise control (ACC), autonomous emergency braking (AEB), blind spot detection (BSD), cross traffic alert (CTA), and rear cross traffic alert (RCTA). They are classified as long-range radar (LRR), mid-range radar (MRR), and short-range radar (SRR) according to the observable distance. The modulation method used in automotive radars is mainly frequency modulated continuous wave (FMCW) [15], and it is divided into slow-chirp FMCW and fast-chirp FMCW depending on the sweep time length and use of down-chirp. The slow-chirp method extracts the up-chirp beat frequency and down-chirp beat frequency using two types of chirp signals, up-chirp and down-chirp. The sum and difference of

these two beat frequencies are used to estimate the range and relative velocity of the target [16]. However, when the slow-chirp signal is used, pairing is required. Thus, recently, the fast-chirp signal has been proposed to address this problem and is used more often [17], [18]. The rest of this dissertation is organized as follows.

First, in Chapter 2, I propose an artificial neural network that can classify road environments. When autonomous cars drive on the road, they encounter various road conditions. In particular, in a road environment with many iron structures, the reflected signal strength is too strong to act as a clutter element, and the target cannot be detected properly. Therefore, it is necessary to apply a clutter suppression algorithm or a target detection algorithm depending on the road environment. In this chapter, the road environment is classified into sound barriers, iron tunnels, typical underground tunnels, and open roads, and a structure of a feedforward neural network that can classify road environments is proposed.

In Chapter 3, I propose a technique to improve the angular resolution using linearly predicted array expansion. The angular resolution is affected by the antenna aperture size. The larger the aperture size, the better the angular resolution. However, a large antenna aperture size requires considerable space and decreases the field of view (FOV). In this chapter, transformation vectors are extracted using the linearity between the received signals in the uniform linear array (ULA) to improve the angular resolution without increasing the antenna aperture size. Virtual received signals are generated by using the extracted transformation vector, and the angular resolution is improved by applying the direction-of-arrival (DOA) estimation algorithm to the actual and virtual received signals.

Finally, in Chapter 4, I propose a method for distinguishing transmission signals using deterministic maximum likelihood (DML) in multi-input multi-output (MIMO) radars. Because MIMO radars use multiple transmit antennas, it is necessary to radiate orthogonal signals to distinguish transmit signals. However, if the signals cannot be distinguished from the receiving antenna, a phenomenon similar to a phase distortion

occurs; thus, the DOA of the target cannot be properly estimated. To solve this problem, in this chapter, DML is applied to the received signals to classify the transmitted signals. In addition, the classified signals are applied to the angle estimation algorithm to improve the DOA estimation.

## **Chapter 2**

# **Road structure classification through artificial neural network for automotive radar systems**

### **2.1 Introduction**

The detection performance of radar is affected by the road environments [19]-[23]. The target detection performance of radar is significantly low in the presence of road structures, such as iron tunnels, sound barriers [24]-[26]. In particular, if the road structure consists of metal, the intensities of the received signals reflected from the road structure are often stronger than those from the vehicle target, which means that the target vehicle cannot be detected appropriately. Because target detection failure can result in fatal accidents, it is important that the radar systems can detect targets even in harsh road environments to ensure safe autonomous driving. To detect targets in such environments, it is required to develop reliable methods for recognizing the road environment.

Some studies have proposed methods to detect road structures using lidar systems or camera systems [27]-[31]; however, the techniques used in these papers are not applicable for radar systems. In [9] and [10], the recognition of road structures using radar have been introduced. In [9], a method to recognize iron tunnels using Shannon

entropy was investigated. In [10], recognition of guard rails, sound barriers, and iron tunnels was discussed. However, they only recognized metal structures and does not classify the road structures. In [11] and [12], a machine learning algorithm was used to classify road structures. They extracted several features and used these features to train a support vector machine (SVM), which is a simple type of machine learning algorithm. However, to use the SVM, it is necessary to extract the representative features well, and the classification performance changes greatly depending on the selected features.

Therefore, I propose a method to classify the types of road structures by using deep learning which can extract unknown features by itself. Road structures are classified based on the fact that the statistical distribution of the received signal strength and fast fourier transform (FFT) magnitude response differ depending on the road structures. Thus, road structures are classified using FFT magnitude response as the input of artificial neural network (ANN). As the output of ANN, sound barriers, iron tunnels, typical underground tunnels, and open roads are set up. I measured received radar signals for the road structure along the Yongin-Seoul Expressway. The performance of the road structure classification system was evaluated by changing the number of receive antenna elements, the number of snapshots used as input data, and the ANN structure. The training, validation, and test sets comprised 70, 15, and 15% of the used data, respectively. With this approach, it was possible to recognize road structures in real time. Compared to [12] in which road structures are classified by direct extraction of features, the proposed method demonstrated that better classification performance can be obtained by using ANN without extracting features. As a result, once the type of structure has been recognized, it is expected that adaptive target detection algorithms can be used for the according road environment.

The remainder of this chapter is organized as follows. A fundamental of slow-chirp FMCW radar and measurement procedures along the specific road structures are introduced in Section 2.2. In Section 2.3, a method of classifying road structures using

ANN is presented. Then, the classification results from the ANN method are analyzed in Section 2.4. Finally, the chapter is concluded in Section 2.5.

## 2.2 System model and target detection in automotive FMCW radar

### 2.2.1 Fundamental of slow-chirp FMCW radar

Assume a single-input and multiple-output FMCW radar system composed of one transmitting antenna and  $N$  identical receiving antenna elements with uniform spacing  $d$ . Then, the transmitted signal in the FMCW radar system can be expressed as follows:

$$S(t) = A_T \cos \left( 2\pi \left( \left( f_c - \frac{BW}{2} \right) t + \frac{BW}{2\Delta T} t^2 \right) \right), \quad (2.1)$$

where  $A_T$  is the amplitude of the transmitted signal,  $f_c$  is the center frequency of the transmitted signal,  $BW$  is the sweep bandwidth of the transmitted signal, and  $\Delta T$  is the sweep time of the transmitted signal. The time-domain received signal reflected from multiple targets,  $R(t)$ , can be expressed as:

$$R(t) = \sum_{l=1}^L A_{R_l} \cos \left( 2\pi \left( \left( f_c - \frac{BW}{2} + f_{d_l} \right) (t - t_{d_l}) + \frac{BW}{2\Delta T} (t - t_{d_l})^2 \right) \right), \quad (2.2)$$

where  $A_{R_l}$  is the amplitude of the received signal from the  $l$ -th target,  $f_{d_l}$  is the doppler frequency reflected at the  $l$ -th target,  $t_{d_l}$  is the time delay corresponding to the  $l$ -th target, and  $L$  is the number of targets. The signal received by the antenna elements is demodulated by a mixer and a low-pass filter. The demodulated signal can then be expressed as:

$$M(t) = \sum_{l=1}^L A_{M_l} \cos \left( 2\pi \left( \frac{BW}{\Delta T} t_{d_l} - f_{d_l} \right) t + 2\pi \left( f_c - \frac{BW}{2} + f_{d_l} \right) t_{d_l} - \frac{\pi BW}{\Delta T} t_{d_l}^2 \right), \quad (2.3)$$

where  $A_{M_l}$  is the amplitude of the demodulated signal from the  $l$ -th target. By applying the Fourier transform to the demodulated signal, I obtain a frequency called the beat frequency, from which I can obtain the target information, such as range and velocity. The beat frequency can be expressed as:

$$f_{b_l} = \frac{BW}{\Delta T} t_{d_l} - f_{d_l}. \quad (2.4)$$

This beat frequency  $f_{b_l}$  can be extracted by applying a peak detection algorithm, such as the constant false alarm rate (CFAR) [32]. The sampled time-domain demodulated signal can be expressed as follows:

$$\begin{aligned} \mathbf{x}_i &= [x_i(1), x_i(2), \dots, x_i(N_s)]^T, \\ &(i = 1, 2, \dots, N_{scan}), \end{aligned} \quad (2.5)$$

where  $N_s$  denotes the number of time samples,  $m$  is the scan index, and  $N_{scan}$  is the total number of scans. The FFT result of  $\mathbf{x}_i$  is expressed as:

$$\begin{aligned} X_i(k) &= \sum_{n=1}^{N_s} x_i(n) e^{-j \frac{2\pi}{N_{FFT}} (k-1)(n-1)}, \\ &(k = 1, 2, \dots, N_{FFT}), \end{aligned} \quad (2.6)$$

where  $N_{FFT}$  denotes the number of points in FFT. Since  $X_i(k)$  is a complex number, the magnitude response is obtained by taking the absolute value for each element, as follows:

$$\mathbf{c}_i = [|X_i(1)|, |X_i(2)|, \dots, |X_i(N_{FFT})|]^T. \quad (2.7)$$

## 2.2.2 Sensor parameter description

I measured radar signals about the road structures along the Yongin-Seoul Expressway. To judge whether it is applicable directly in an actual road environment, the experiment was conducted in various environments while driving on an actual road rather than an ideal environment. Furthermore, the experiment was performed under various conditions while changing the ego velocity continuously and with varying distances from

the target. The measurements were conducted using a long-range radar manufactured by Mando Corporation. This system has a FoV from  $-10^\circ$  to  $10^\circ$  and the maximum detection range of 250 m. The number of transmit and receiving antenna elements were 1 and 4, respectively, the antenna spacing between each receiving antenna element was  $1.8\lambda$  where  $\lambda$  is the wavelength of the transmitted signal, and FFT length is 2048. In operation, the system transmitted a 76.5 GHz FMCW radar signal with a bandwidth of 500 MHz and a 10 ms sweep time for the up- and down-chirping. One scan takes 100 ms, consisting of up- and down-chirping times of 10 ms and signal processing times of 90 ms.

### 2.2.3 Target detection in various road structures

In this section, I discuss the FFT results for different road environments. General elements in driving environments, such as sound barriers, iron tunnels, typical underground tunnels, and open roads, are shown in Fig. 2.1. A total of 600 scans (i.e., from  $c_1$  to  $c_{600}$ ) acquired while driving for 1 min in four different road environments are shown in Fig. 2.2. The  $x$  axis can be converted to time. If the relative velocity between the target and the radar-equipped vehicle is zero,  $y$  axis can be converted to distance. Sound barriers appear from about the 300-th scan to the 600-th scan in Fig. 2.2 (a), and the horizontally curved lines indicate other vehicles driving in the FOV of our radar. If a target vehicle is faster than the radar-equipped vehicle, the up slope curve extends from the lower left to the upper right. If the target vehicle is slower than the radar-equipped vehicle, the down slope curve extends from the upper left to the lower right. Because there are a lot of targets, only a few targets that are noticeable in Fig. 2.2 are marked. In case of stationary road structures, curves appear as lines having tangential slopes proportional to the velocity of the radar-equipped vehicle. If the radar-equipped vehicle is moving at a constant velocity, lines are straight. In Fig. 2.2 (a), straight lines appear in the frequency domain when the vehicle enters the section with sound barriers. In Fig. 2.2 (b), the signals reflected by the metal structures in the iron tunnel are

dominant. Thus, the target vehicles could not be accurately detected beyond a certain critical distance. While iron tunnels possess similar characteristics to the sound barrier because they are both made of iron, the received signals reflected from iron tunnels are stronger than those reflected from the sound barriers. In Fig. 2.2 (c), the 200-th to the 600-th scan is the inside of a typical underground tunnel, and several unwanted reflections occur due to the tunnel structure. However, since the typical underground tunnel is not made of iron, the intensities of the reflected signals are relatively weak; thus, the preceding vehicle is detected fairly well. In Fig. 2.2 (d), the effect of the median strip appears periodically, but this is much less likely to act as clutter than the other road structures. The targets are well detected on the open road, unlike environments having metal road structures. As shown in Fig. 2.2, when 600 scans are obtained, the characteristics of the road structures are distinct enough to tell the difference between them.

Instead, the instantaneous FFT magnitude response is also enough to tell the difference. Instantaneous FFT magnitude responses of a single scan for each road environment are shown in Fig. 2.3. The red circles in the figure represent the signals that are reflected from the target vehicles, while the red lines indicate the threshold lines using order statistics (OS)-CFAR [33], one of the CFAR algorithms. If an FFT magnitude is greater than the CFAR threshold, the point is recognized as a meaningful target. Thus, in an ideal situation, all of the red circles should be above the red line. Figures 2.3 (a) and 2.3 (b) show multiple reflected signals from the road structures, which cause the desired targets to not be properly detected. In addition, the intensities of the reflected signals in the iron tunnel are stronger than those in other road environments. As shown in Fig. 2.3 (c), non-target signals are also received while the vehicle is in a typical underground tunnel. However, since a typical underground tunnel is not made of iron structures, the targets are well detected compared to other environments such as iron tunnels or sound barriers. In Fig. 2.3 (d), unlike metal road structures, the targets are easily detected on the open road. Generally, the number of vehicles does not greatly

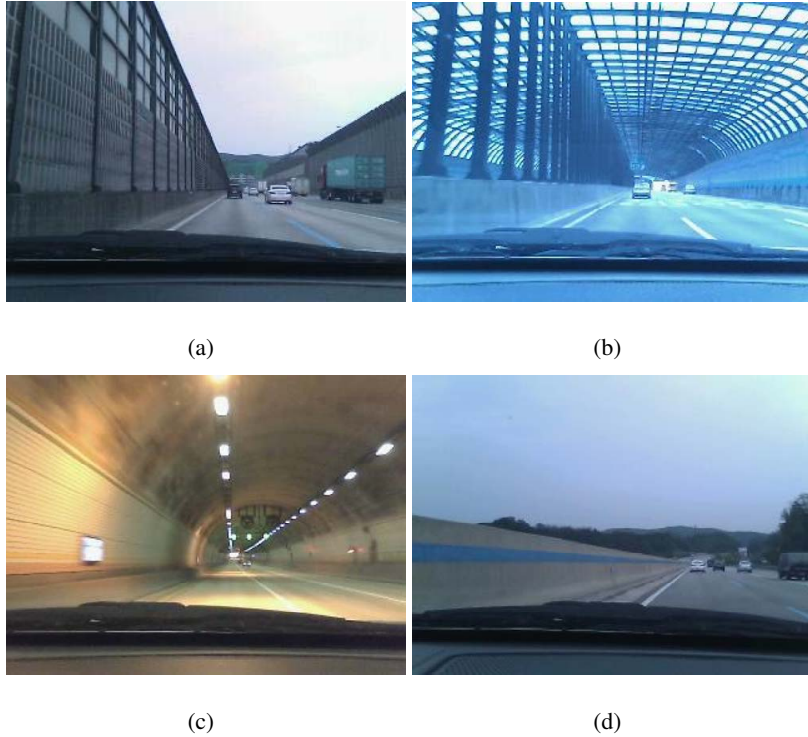


Figure 2.1: Snapshots of (a) sound barrier, (b) iron tunnel, (c) typical underground tunnel, and (d) open road.

affect the road structure classification performance, because the reflection signal by the road structure is more intense than the reflection signal by other vehicles. Moreover, I did not consider the influence of the number of vehicles and the experiment was carried out in situations where the number of vehicles was varied. Based on these results, the received signals reflected from each structure have unique characteristics even during one scan. Thus, these characteristics can be used to distinguish between the different structures. Since the different metal density of road structure results in the different intensities of the reflected signals, instantaneous FFT magnitude responses can be used to classify the types of road structures.

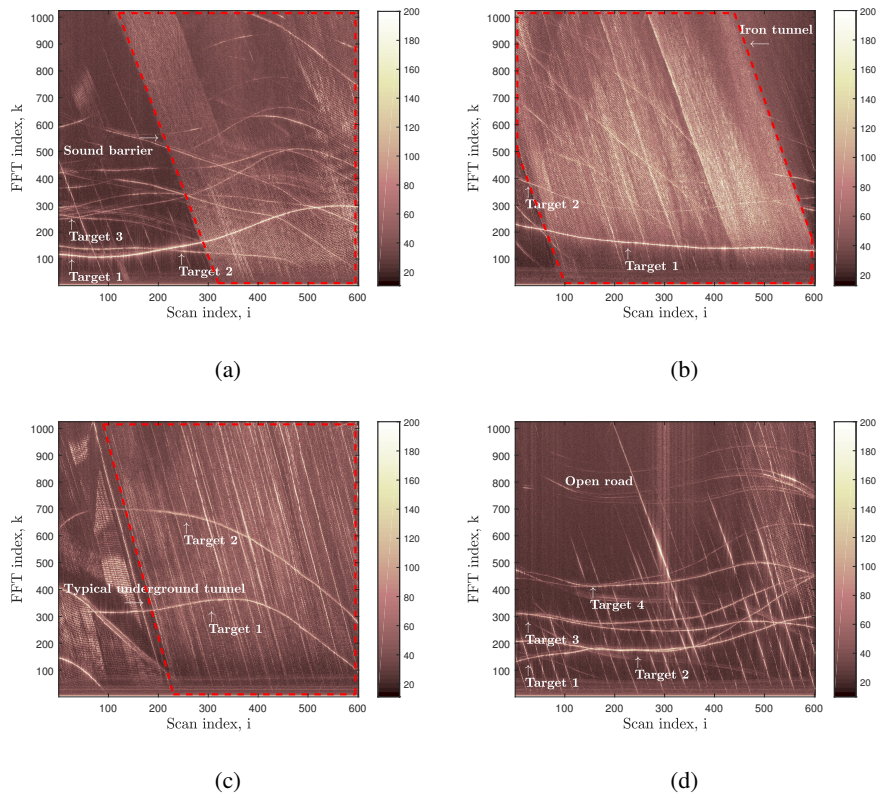


Figure 2.2: Accumulated FFT data for (a) sound barrier, (b) iron tunnel, (c) typical underground tunnel, and (d) open road.

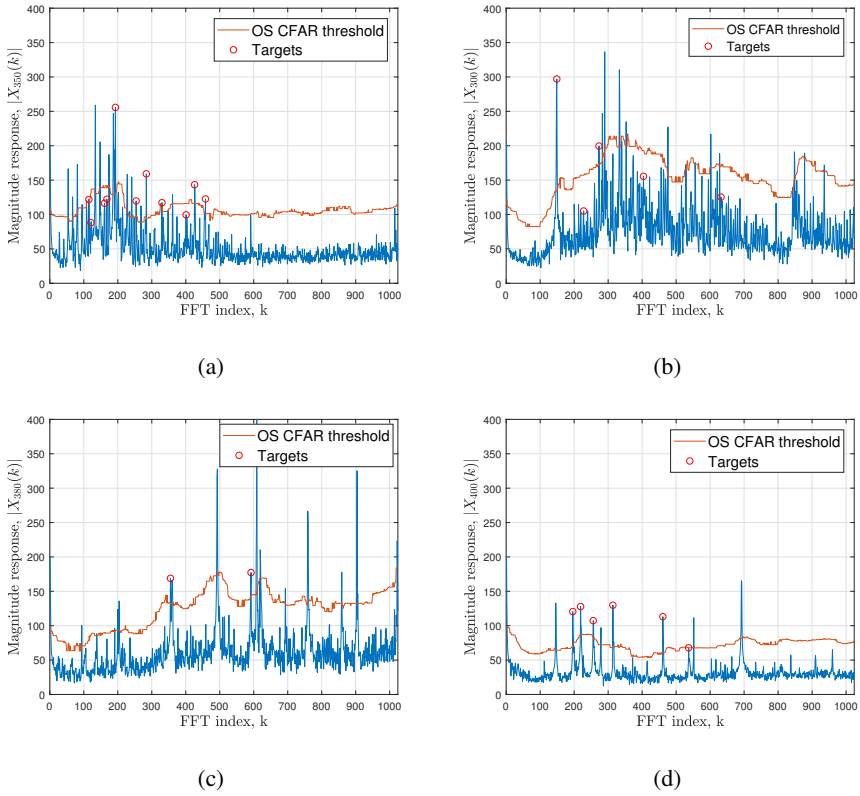


Figure 2.3: Instantaneous FFT magnitude responses for: (a) sound barrier, (b) iron tunnel, (c) typical underground tunnel, and (d) open road.

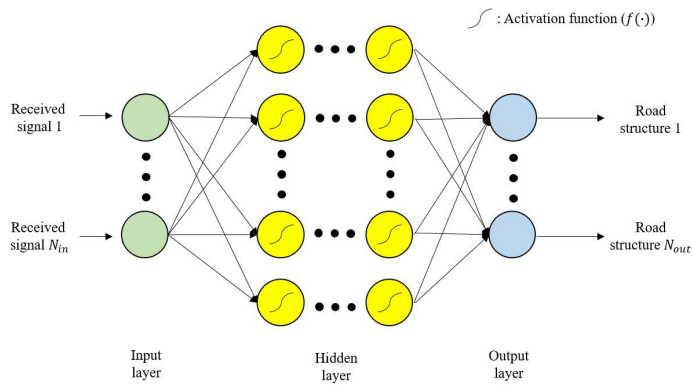


Figure 2.4: Framework of the proposed artificial neural network

## 2.3 Road structure classification via ANN

An ANN is a type of machine learning algorithms. While the performance of most machine learning techniques depends on how features are extracted from the received data, deep learning algorithms automatically extract meaningful features through the training process and are able to identify hidden features that otherwise would not be found.

ANN algorithms used for target classification include convolutional neural network [34], [35] and recurrent neural network [36]. However, they are not suitable for automotive radar that needs real-time signal processing. The computational complexity of CNN is  $O(\sum_{l=1}^{N_{layer}} c_l \cdot s_l^2 \cdot n_l \cdot m_l^2)$ , where  $l$  is the index of a CNN layer,  $N_{layer}$  is the number of convolutional layers, and  $c_l$  is the number of input channels of the  $l$ -th layer. In addition,  $s_l$  is the spatial size of the filter,  $n_l$  is the number of filters in the  $l$ -th layer, and  $m_l$  is the spatial size of the output feature map [37]. The computational complexity of RNN is  $O(P^2Q)$  per epoch, where  $P$  is the number of units in a RNN layer and  $Q$  is the total number of time steps [38].

Thus, ANN known as PatternNet, which is relatively simple in network structure and has low complexity, is used to classify and recognize road structures [39]–[41]. A radar-equipped vehicle is used to gather time domain received signal data across four different road environments, namely, sound barrier, iron tunnel, typical underground tunnel, and open road. Then, the frequency domain signal is obtained by performing FFT on the signal received in the time domain. Next, the magnitude responses of FFT are compared to each other. In this chapter, I employ a multilayer neural network called PatternNet. The structure of PatternNet with several hidden layers is shown in Fig. 2.4. Learning of the multilayer artificial neural network is performed via a backpropagation algorithm that is divided into four stages [42]. Figure 2.5 shows the flowchart of the proposed neural network. The specific description of each stage in the flowchart is as follows. The first stage is to initialize the network. This requires each weight and threshold value in each neuron to be assigned within a certain range. The second stage

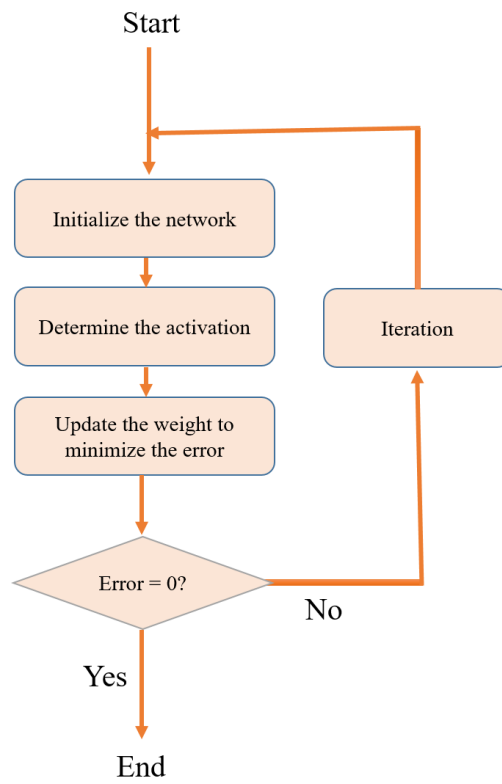


Figure 2.5: Flowchart of the proposed artificial neural network

is to determine the activation. The function from the input layer to the hidden layer can be expressed as follows:

$$h_r(p) = f\left(\sum_{q=1}^{N_{in}} g_q(p)w_{qr}(p) - b_r\right), \quad (2.8)$$

$(r = 1, 2, \dots, N_{hidden})$

where  $h_r(p)$  and  $g_q(p)$  denote the values of the  $r$ -th node of the hidden layer and the  $q$ -th node of the input layer, respectively. The  $q$ -th node of the input layer contains  $|X_i(q)|$  corresponding to the  $q$ -th value of the FFT magnitude response. In addition,  $w_{qr}(p)$  is the weight between  $h_r(p)$  and  $g_q(p)$ ,  $b_r$  is the bias of  $h_r(p)$ ,  $p$  is the iteration index,  $N_{in}$  is the total number of input nodes,  $N_{hidden}$  is the total number of hidden nodes, and the function  $f(\cdot)$  denotes an activation function. As in (2.9), the calculation process from the hidden layer to the output layer can be expressed as:

$$o_s(p) = f\left(\sum_{r=1}^{N_{hidden}} h_r(p)w_{rs}(p) - b_s\right), \quad (2.9)$$

$(s = 1, 2, \dots, N_{out})$

where  $o_s(p)$  denotes the value of the  $s$ -th node of the output layer,  $w_{rs}(p)$  is the weight between  $o_s(p)$  and  $h_r(p)$ ,  $b_s$  is the bias of  $o_s(p)$ , and  $N_{out}$  is the total number of output nodes. Here, I have performed experiments to classify four road structures, so  $N_{out}$  is 4. Once the activation has been determined, the weights are learned in the third stage. The goal here is to update the weight to minimize the magnitude of the error, which can be expressed as:

$$E(p) = \frac{1}{2} \sum_{s=1}^{N_{out}} \left(\hat{o}_s(p) - o_s(p)\right)^2, \quad (2.10)$$

where  $\hat{o}_s(p)$  is the  $s$ -th actual output value. Here, the value of  $w_{rs}(p)$  that minimizes  $E(p)$  can be expressed as:

$$\begin{aligned} w_{rs}(p+1) &= w_{rs}(p) - \eta \frac{\partial E(p)}{\partial w_{rs}(p)} \\ &= w_{rs}(p) - \eta \delta_s^o(p) h_r(p), \end{aligned} \quad (2.11)$$

where

$$\delta_s^o(p) = o_s(p)(1 - o_s(p))(\hat{o}_s(p) - o_s(p)), \quad (2.12)$$

and  $\eta$  is the step size. The term  $w_{qr}(p)$  can be updated in the same way. This can be expressed as:

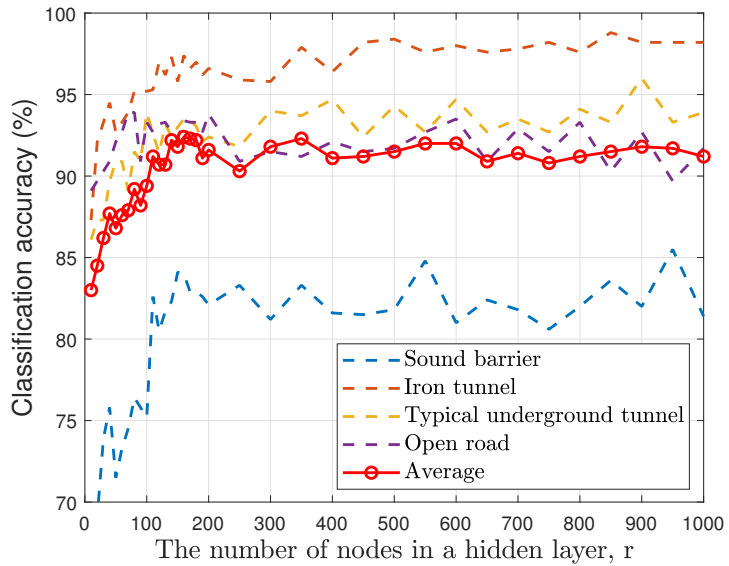
$$\begin{aligned} w_{qr}(p+1) &= w_{qr}(p) - \eta \frac{\partial E(p)}{\partial w_{qr}(p)} \\ &= w_{qr}(p) - \eta h_r(p)(1 - h_r(p)) \\ &\quad \times \sum_{s=1}^{N_{out}} w_{rs}(p) \delta_s^o(p) g_q(p). \end{aligned} \quad (2.13)$$

Finally, as an iterative stage,  $p$  is increased and the activation and weight learning stages are repeated until the error reaches zero in all epochs.

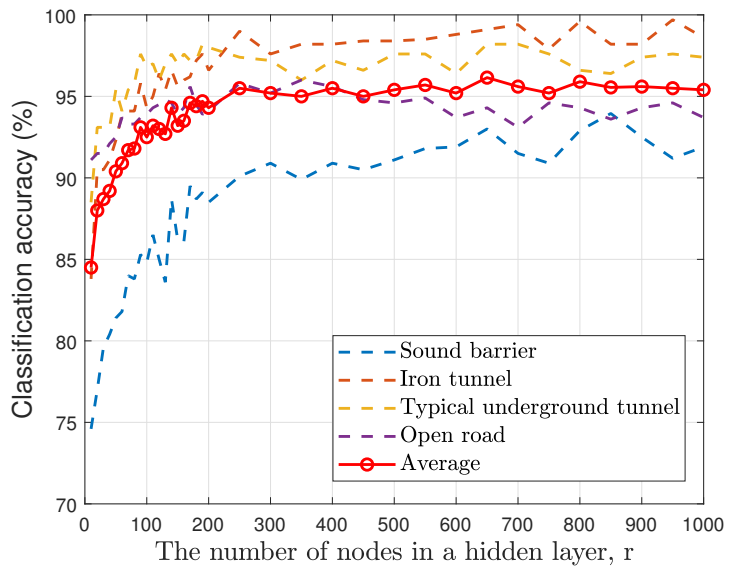
## 2.4 Target classification results

This section presents the classification performance when ANN is applied to experimental data obtained using an actual automotive radar system. The experiments were conducted on the Yongin-Seoul Expressway, and the experimental data consist of 13,680 scans to verify the deep learning performance, of which 70%, 15%, and 15% of the data is reserved for training, validation, and test set, respectively. The FFT magnitude response from (2.7) is employed as the input to PatternNet. The output is a  $4 \times 1$  vector since I classify four types of road structures. The output layer is configured as a competitive layer because at least one of the road environments must be recognized in each snapshot. The following results are all based on the FFT magnitude response obtained from four antenna elements. This is because the classification performance is very poor when the phase part of the FFT result or the FFT result itself is directly used as the input.

The performance of deep learning depends on the number of hidden layers, number of nodes, and type of activation function. To ascertain the effects of each factor,



(a)

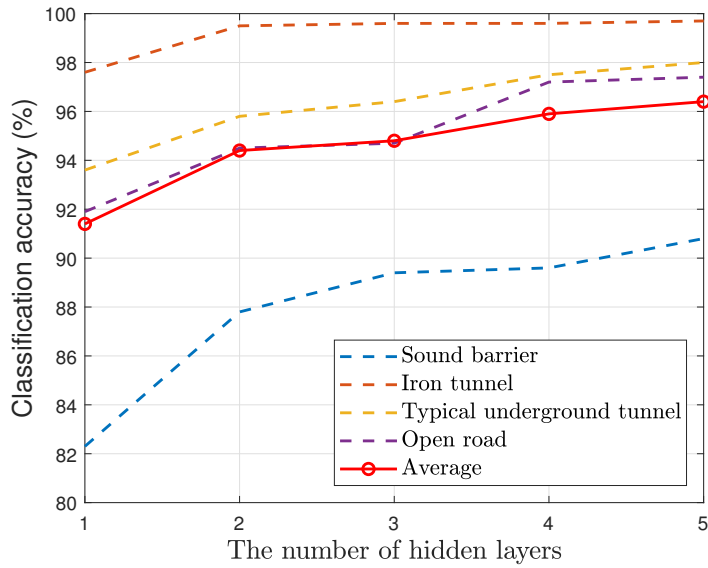


(b)

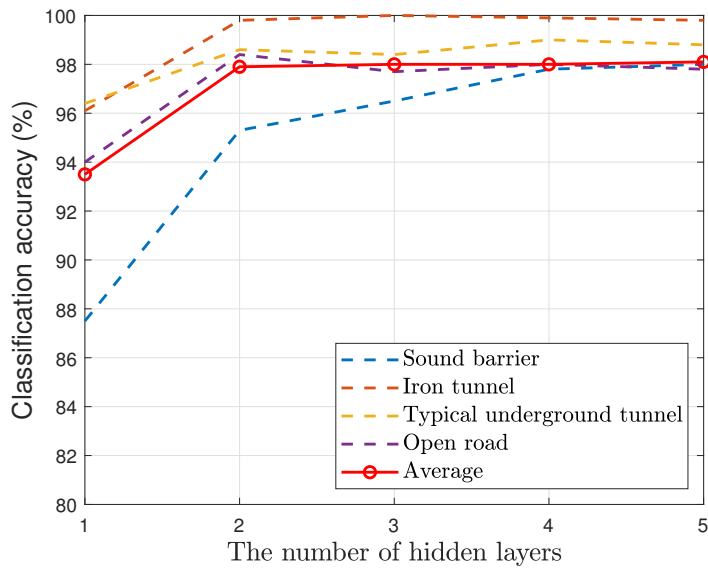
Figure 2.6: Classification performance with an increasing number of nodes in the hidden layer when the activation function is: (a)  $\tanh$  and (b)  $ReLU$

the road structure classification process is conducted while varying each factor and monitoring the results. The classification accuracy based on the number of nodes in the hidden layer when one hidden layer is used is shown in Fig. 2.6. In Figures 2.6 (a) and 2.6 (b), the  $\tanh$  and  $ReLU$  functions are used as the activation functions, respectively, where the  $\tanh$  function can be expressed as  $f(x) = \frac{e^x - e^{-x}}{e^x + e^{-x}}$ ,  $ReLU$  function can be expressed as  $f(x) = \max(0, x)$  [43]. The results from testing with different number of hidden layer nodes show that, as the number of nodes increases, the classification performance increases linearly, and when the number of nodes exceeds a certain number, the classification accuracy is saturated. In addition, when the  $\tanh$  function is used, the classification performance is saturated when the number of nodes is about 160. When the  $ReLU$  function is used, the classification performance is saturated when the number of nodes is about 250. The effect of the number of layers is shown in Fig. 2.7. In this test, the number of nodes in the hidden layer is changed according to the classification performance. In Fig. 2.7 (a), the classification performance is enhanced as the number of hidden layers is increased. In Fig. 2.7 (b), if the number of layers exceeds two, the classification performance is saturated. In addition, if batch normalization is not applied properly, the classification performance deteriorates as the number of layers increases. As shown in Figs. 2.6 and 2.7,  $ReLU$  is better than  $\tanh$  in terms of classification performance. Thus, all following experiments were carried out using  $ReLU$  as the activation function in the road structure classification process.

Next, the variation in performance is analyzed versus the number of receiving antenna elements  $N$ . An  $N_{FFT} \times N$  matrix contains the up-chirp FFT magnitude response of the received signals, where  $N_{FFT} = 1024$  and  $N = 1, 2, 3,$  or  $4$ . The number of hidden layer and the number of node are set based on the previous experimental results. The number of hidden layer is two and the number of nodes in the hidden layer is 250. A  $ReLU$  function is used as the activation function in the hidden layer. The results of classifying road environments by applying the ANN to actual



(a)



(b)

Figure 2.7: Classification performance with an increasing number of hidden layers when the activation function is: (a)  $\tanh$  and (b)  $ReLU$

experimental data are listed in Table 2.1. Increasing the number of receiving antenna elements also improved the road structure classification performance. Furthermore, the classification accuracy for classifying iron tunnels is almost 100% because they exhibit distinct characteristics compared to other road environments. Sound barriers are not as distinctive as other road structures. Therefore, their classification performance is the lowest among the four road environments.

The different types of roads can exhibit similar characteristics when one FFT magnitude response is used. In order to prevent this, the deep learning process is executed with three consecutive magnitude responses (e.g.,  $c_i$ ,  $c_{i+1}$ , and  $c_{i+2}$ ). Thus, input data size is  $1024 \times 12$ . Table 2.2 shows the results of deep learning with three consecutive FFT magnitude responses inserted simultaneously as the input data. In Table 2.2, the first row represents the actual road structure and the first column represents the road structure estimated from the test result. In these results, the number of hidden layers is two and the number of hidden layer nodes is 250. In addition, a *ReLU* function is used as the activation function. In this test, all of the iron tunnels are properly classified, while, for the sound barriers, nearly 3.5% of the test data are incorrectly recognized as typical underground tunnels. In addition, I confirmed how the classification performance varies depending on the number of scans used as input to the neural network. The classification results according to the number of scans are shown in Table 2.3. As the number of scans used increases, the classification performance continues to improve, but the rate of performance increase is low. Consequently, the total classification accuracy is 98.8%. The average classification performance is enhanced by 2.5%p when more than one FFT magnitude response is used.

Finally, I compare the classification performance between two input settings; the FFT magnitude response without any feature extraction, and extracted features of the FFT magnitude response. Similar to the previous study [12], the mean, variance, skewness, and kurtosis of the FFT magnitude responses are used as the features. When the features are extracted and used as the input to ANN, the input size of ANN was  $4 \times 4$ .

Table 2.1: Classification performance according to the number of antenna elements.

Input data size	Sound barrier	Iron tunnel	Typical underground tunnel	Open road	Average
1024 x 1	89.1%	99.3%	99.0%	98.0%	<b>96.3%</b>
1024 x 2	92.5%	99.9%	97.8%	97.1%	<b>96.8%</b>
1024 x 3	92.9%	99.5%	98.2%	99.4%	<b>97.5%</b>
1024 x 4	96.9%	99.3%	98.9%	97.1%	<b>98.0%</b>

Table 2.2: Confusion matrix when using 3 consecutive scans.

Estimated class / Actual class	Sound barrier	Iron tunnel	Typical underground tunnel	Open road	Average
Sound barrier	<b>95.9%</b>	0.0%	2.1%	0.4%	
Iron tunnel	0.6%	<b>100.0%</b>	0.0%	0.1%	
Typical underground tunnel	3.5%	0.0%	<b>97.9%</b>	0.7%	
Open road	0.0%	0.0%	0.0%	<b>98.8%</b>	
Average					<b>98.2%</b>

Table 2.3: Classification performance according to the number of scans.

# of input scans	Sound barrier	Iron tunnel	Typical underground tunnel	Open road	Average
1	96.9%	99.3%	98.9%	97.1%	<b>98.0%</b>
3	95.9%	100%	97.9%	98.8%	<b>98.2%</b>
5	95.7%	100%	98.7%	98.1%	<b>98.2%</b>
10	95.9%	99.8%	100%	97.7%	<b>98.3%</b>
20	96.7%	100%	99.9%	98.6%	<b>98.8%</b>

Table 2.4: Confusion matrix when the deep learning is performed using the suggested features in [12].

Estimated class / Actual class	Sound barrier	Iron tunnel	Typical underground tunnel	Open road	Average
Sound barrier	<b>61.0%</b>	1.1%	3.9%	4.7%	
Iron tunnel	0.5%	<b>94.6%</b>	1.2%	0.0%	
Typical underground tunnel	34.3%	4.3%	<b>94.5%</b>	1.6%	
Open road	4.2%	0.0%	0.4%	<b>93.7%</b>	
Average					<b>87.6%</b>

The road structure classification results for the deep learning using the above listed features is shown in Table 2.4. The data used for the classification of road structures are measured by radar as in [12]. The input of the classifier is the FFT magnitude response of the received time-domain signal, and no further preliminary processing was done on the input, such as OS-CFAR. Next, for the performance comparison with the SVM, the road structure classification was performed using the feature and SVM proposed in [12]. Table 2.4 shows the classification results using the Gaussian kernel. The mean, variance, coefficient of variance, skewness, and kurtosis of the received signal are used as features. When SVM is used, the classification performance is much lower than ANN algorithm proposed in this chapter. Particularly, in the case of the sound barrier, the classification accuracy is less than 50%. The experiment uses two hidden layer and 250 nodes and *ReLU* is used as the activation function. The detection performance for a typical underground tunnel and open road is similar to that when the FFT magnitude response is used as the input to artificial neural network; however, the detection performance of an iron tunnel and sound barrier is significantly worse. In the case of the sound barrier, the extracted features are not sufficiently distinct compared with those of the other road structures, so they could not be accurately classified. This result shows improvement of classification performance by over 14%p compared with the results using support vector machine.

Table 2.5: Confusion matrix when the support vector machine with a Gaussian kernel is performed using the suggested features in [12].

<b>Estimated class / Actual class</b>	Sound barrier	Iron tunnel	Typical underground tunnel	Open road	Average
Sound barrier	<b>46.8%</b>	5.2%	1.9%	2.9%	
Iron tunnel	48.6%	<b>91.2%</b>	5.6%	4.1%	
Typical underground tunnel	1.3%	3.5%	<b>92.6%</b>	0.0%	
Open road	4.5%	0.0%	0.0%	<b>93.1%</b>	
Average					<b>84.0%</b>

## 2.5 Conclusion

In this chapter, I classified road structures by applying an artificial neural network to the frequency domain signals received from various road environments. I evaluated how the classification performance varied with the number of hidden layers, the number of nodes in a hidden layer, and the types of activation function. Using the results obtained from various experiments, I propose which neural network structure suits the road structure classification. In addition, I confirmed how classification performance varies with input data size by changing the number of antenna elements and the number of scans. Based on these results, it was demonstrated that the proposed method was able to effectively classify road structures without extracting features from the measured data in advance. When the deep learning method was applied, the four different road environments were accurately recognized with an average accuracy of 98.8%. The results of this experiment confirm the proposed deep learning method can be used to classify various road structures. Using these results, I can apply a target detection algorithm suitable for each road environment. In future research, I will classify more diverse road structures existing in the urban areas, and additionally attempt to recognize transition regions.

## **Chapter 3**

# **Enhanced DOA Estimation Using Linearly Predicted Array Expansion for Automotive Radar Systems**

### **3.1 Introduction**

DOA estimation algorithms such as the Bartlett algorithm [44] or multiple signal classification (MUSIC) [45] are being employed in automotive radar systems to obtain the angular locations of detected targets. However, when multipath is generated in a variety of ways and coherent sources are present, the target position is not correctly detected. To solve this problem, many algorithms for estimating the DOA of the target using spatial smoothing have been proposed [46]–[48].

In general, when estimating the DOA of a target with the array antenna system, narrow main beamwidth and low side lobes are required to achieve fine angular resolution [49], [50]. When the main beamwidth is wide, the targets simultaneously located within the beamwidth cannot be distinguished. To obtain a narrow main beam, the number of antenna elements in the array must be increased, which increases the production costs. Thus, signal processing techniques are needed to improve the DOA estimation performance without increasing the number of actual antenna elements.

For instance, various studies have been conducted to enhance the angular reso-

lution of array antenna system with a small number of antenna elements [51]–[58]. Specifically, methods to increase the number of antenna elements using array interpolation have been proposed in [51]–[56]. Most interpolation techniques assume that coherent sources exist. Therefore, interpolation was performed to convert non-uniform linear array (NLA) to ULA and to apply the spatial smoothing technique [51], [53]. These methods require the setup of an observation interval, called a sector, before estimating the DOA. In other words, such methods can be applied only when the angular location of the target is approximately known. If the sector is set incorrectly and the target to be found is located outside the sector, the target cannot be detected properly. Thus, the sector should be set wide at first because it does not know the locations of the targets. Subsequently, since the angles of the targets are estimated while gradually narrowing the sector with respect to the region where the targets exist, the calculation complexity is increased by the number of times the sector is set. Moreover, array extrapolation has been proposed to enhance the angular resolution in [57], [58]. However, the methods in [57], [58] require updating the transformation vector whenever the signals are extrapolated. Thus, a more efficient and concise method has to be proposed. Furthermore, a limit to improving the angular resolution exists because the number of extrapolated antenna elements can only be increased to twice that of the physical antenna elements.

In this chapter, I propose a linearly predicted array expansion method to enhance both the angular resolution and estimation accuracy of the DOA estimation algorithm. In our proposed method, I extract the transformation vector that represents the linear relation among received signals and generate extrapolated elements outside the physical array antenna elements. Moreover, the proposed array expansion method consists of forward and backward array expansion, which generates elements to the left and right sides of the array antenna. When using both the original and extrapolated signals, the angular locations of targets can be estimated with a higher angular resolution. The performance of our proposed method is evaluated through simulations and actual

experimental results using a commercial automotive radar sensor to verify its applicability. In terms of the root-mean-square error (RMSE) and resolution probability, I found that the proposed method showed higher angular resolution and estimation accuracy compared to the conventional methods.

In addition to extending the antenna by extrapolation or interpolation, many methods have been proposed to achieve finer angular estimation performance using a small number of antennas. For example, there are minimum redundancy array [59], [60], nested array [61], [62], and co-prime array [63], [64]. They have the advantage of being able to detect more targets than the number of antennas, with limited antenna aperture size and number of antennas by maximizing degree of freedom. However, if the antennas are expanded using the proposed method, I can have better angular resolution than those using the conventional optimal NLA.

In [54], a disadvantage occurs in that it is necessary to newly acquire the position of an appropriate expanded antenna elements according to the positions of the targets to obtain a good angle estimation performance. However, in our proposed method, a uniform linear array antenna is used to generate the expanded antenna elements. Since ULA is used, there is an advantage that it is robust against multipath as compared with NLA-based techniques [65], [66]. Furthermore, the advantage of our method is that the positions of expanded antenna elements need not be calculated at that time. In addition, unlike the methods in [51]–[56], proposed method can estimate the position of targets at once without having to set the sector, such that the target position can be detected with little calculation irrespective of the target location. In [57] and [58], the transformation vector is obtained using the covariance matrix of the received signal. With this method, the number of expanded antennas can only be generated as twice as many as the actual number of antennas. If the number of extrapolated antenna elements exceeds twice the number of physical antenna elements, the additional extrapolated received signals are generated using only the extrapolated signals. When the conventional extrapolation generates the extrapolated signals, the extrapolated signal

values are inaccurate because the errors continue to be reflected. In this chapter, since the expanded antenna elements are generated using the linear least-squares method, it is possible to generate more accurate expanded antenna elements than the conventional method by minimizing the error of the received signal. As a result, the proposed method can obtain better angular resolution and angle estimation accuracy than the conventional methods.

The rest of this chapter is organized as follows. First, a signal model for a ULA antenna and the basic DOA estimation algorithm are presented in Section 3.2. In Section 3.3, the proposed DOA estimation method using linearly predicted array expansion is presented. Furthermore, simulation results using the proposed method and conventional methods are analyzed in Section 3.4, and the performance of the proposed method is also examined with the actual measurement data in Section 3.5. Finally, I conclude this chapter in Section 3.6.

## 3.2 DOA Estimation in Array Antenna System

### 3.2.1 Signal Model for ULA Antenna

I assume a single-input multiple-output antenna system, which is composed of one transmitting antenna and  $N$  identical receiving antenna elements with uniform spacing  $d$ . If the transmitted signal is reflected from  $L$  targets, the received signal vector can be expressed as

$$\begin{aligned} \mathbf{x}(k) &= \mathbf{A}\mathbf{s}(k) + \mathbf{n}(k) \\ &= [x_1(k), x_2(k), \dots, x_N(k)]^T, \end{aligned} \quad (3.1)$$

where  $k$  indicates the time index for the sampled signals and  $[\cdot]^T$  denotes the transpose operator. In addition,  $\mathbf{A} = [\mathbf{a}(\theta_1), \mathbf{a}(\theta_2), \dots, \mathbf{a}(\theta_L)]$  is a steering matrix composed

of steering vectors. The steering vector is given by

$$\mathbf{a}(\theta_l) = [e^{j\frac{2\pi}{\lambda}d_1 \sin \theta_l}, e^{j\frac{2\pi}{\lambda}d_2 \sin \theta_l}, \dots, e^{j\frac{2\pi}{\lambda}d_N \sin \theta_l}]^T$$

$$(l = 1, 2, \dots, L), \quad (3.2)$$

where  $\lambda$  is the wavelength of the transmitted signal,  $d_i$  ( $i = 1, 2, \dots, N$ ) denotes the distance from the first antenna to the  $i$ -th antenna element (i.e.,  $d_i = (i - 1)d$ ).  $\theta_l$  denotes the angle of the  $l$ -th target, which is defined as the angle from the boresight direction of the array antenna. Moreover,  $\mathbf{s}(k) = [s_1(k), s_2(k), \dots, s_L(k)]^T$  and  $\mathbf{n}(k) = [n_1(k), n_2(k), \dots, n_N(k)]^T$  denote the incident signal and the zero-mean white Gaussian noise vectors, respectively. Here, I assume that the incident signal and noise components are uncorrelated and the power of  $\mathbf{n}(k)$  is  $E[\mathbf{n}(k)\mathbf{n}^H(k)] = \sigma_n^2 \mathbf{I}$ , where  $E[\cdot]$  and  $(\cdot)^H$  denote the expectation and conjugate transpose operators, respectively.

### 3.2.2 Bartlett Algorithm

In this chapter, I evaluate the performance of the proposed array expansion method mainly using the Bartlett DOA estimation algorithm. In the Bartlett algorithm, the weight vector  $\mathbf{w}^*$  that maximizes the output signal power of the array antenna has to be determined [67] as

$$\begin{aligned} \mathbf{w}^* &= \arg \max_{\mathbf{w}} E \left[ |\mathbf{w}^H \mathbf{x}(k)|^2 \right] \\ &= \arg \max_{\mathbf{w}} \left\{ E \left[ |s(k)|^2 \right] |\mathbf{w}^H \mathbf{a}(\theta)|^2 + \sigma_n^2 \|\mathbf{w}\|_2^2 \right\}, \end{aligned} \quad (3.3)$$

where  $|\cdot|$  denotes the absolute value and  $\|\cdot\|_2$  denotes the  $l_2$ -norm. This assumes that the power of the weighted noise component is constant, i.e.,  $\|\mathbf{w}\|_2^2$  has to be set as unity. Thus, the optimal solution of (3.3) is given by

$$\mathbf{w}^* = \frac{\mathbf{a}(\theta)}{\sqrt{\mathbf{a}^H(\theta)\mathbf{a}(\theta)}}, \quad (3.4)$$

and the power of the weighted output can be expressed as

$$\begin{aligned}
 P(\theta) &= E \left[ \left| \mathbf{w}^{*H} \mathbf{x}(k) \right|^2 \right] \\
 &= \frac{\mathbf{a}^H(\theta) \mathbf{R}_{xx} \mathbf{a}(\theta)}{\mathbf{a}^H(\theta) \mathbf{a}(\theta)},
 \end{aligned} \tag{3.5}$$

where  $\mathbf{R}_{xx} = E[\mathbf{x}(k)\mathbf{x}^H(k)]$  is the autocorrelation matrix of the received signal vector given by (3.1). Because power  $P(\theta)$  has the highest value at the angle where the target is located, the angle of the target can be estimated by searching  $\theta$  [67].

In practice, the exact statistics for  $\mathbf{s}(k)$  and  $\mathbf{n}(k)$  are unknown. If processes  $\mathbf{s}(k)$  and  $\mathbf{n}(k)$  are considered as ergodic, the ensemble average can be replaced by the time average. Thus, I can estimate  $\mathbf{R}_{xx}$  using time-averaged autocorrelation matrix as

$$\hat{\mathbf{R}}_{xx} = \frac{1}{K} \sum_{k=1}^K \mathbf{x}(k)\mathbf{x}^H(k), \tag{3.6}$$

where  $K$  is the number of time samples used to calculate the matrix. The number of time samples is related to the range resolution of the radar system.

### 3.3 Proposed Linearly Predicted Array Expansion

In this section, an advanced DOA estimation method is proposed to enhance the angular resolution of the Bartlett algorithm. The method extracts the linear relation among received signals, and the extrapolated signals are generated outside the regions covered by the actual array antenna. However, because the proposed method is based on the linearity of the phase of the received signals in uniform linear array system, it is not applicable to nonuniform linear arrays. The extrapolation includes forward and backward linearly predicted array expansions. Then, using both the original and extrapolated signals, I estimate the angle of the target.

#### 3.3.1 Forward Linearly Predicted Array Expansion

In the forward linearly predicted array expansion, I extrapolate the received signal beyond the  $N$ -th antenna element, as illustrated in Fig. 3.1 (a). To generate the signal

at the  $(N + 1)$ -th antenna element located at distance  $Nd$  to the right of the first antenna element, the linear relation among the  $N$  received signals is extracted. If the  $K$  time-sampled received signal vector at the  $i$ -th antenna element is expressed as

$$\mathbf{x}_i = [x_i(1), x_i(2), \dots, x_i(K)]^T$$

$$(i = 1, 2, \dots, N). \quad (3.7)$$

Since the uniform linear array is used, linearity exists between the phases of the received signals. Thus,  $\mathbf{x}_N$  can be expressed as a linear combination of  $\mathbf{x}_1, \mathbf{x}_2, \dots, \mathbf{x}_{N-1}$ :

$$\mathbf{x}_N \approx [\mathbf{x}_1, \mathbf{x}_2, \dots, \mathbf{x}_{N-1}] \mathbf{u}_f = \mathbf{X}_f \mathbf{u}_f = \tilde{\mathbf{x}}_N. \quad (3.8)$$

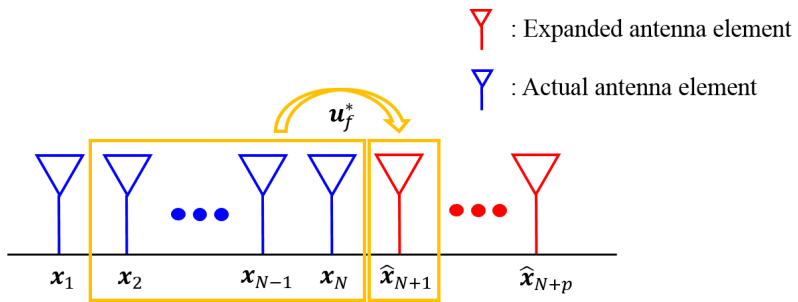
Here,  $\mathbf{u}_f$  is the vector composed of coefficients for the linear combination and  $\mathbf{X}_f = [\mathbf{x}_1, \mathbf{x}_2, \dots, \mathbf{x}_{N-1}]$ . To find the coefficient vector, I solve the least squares problem which is defined as

$$\mathbf{u}_f^* = \arg \min_{\mathbf{u}_f} \|\mathbf{x}_N - \tilde{\mathbf{x}}_N\|_2^2, \quad (3.9)$$

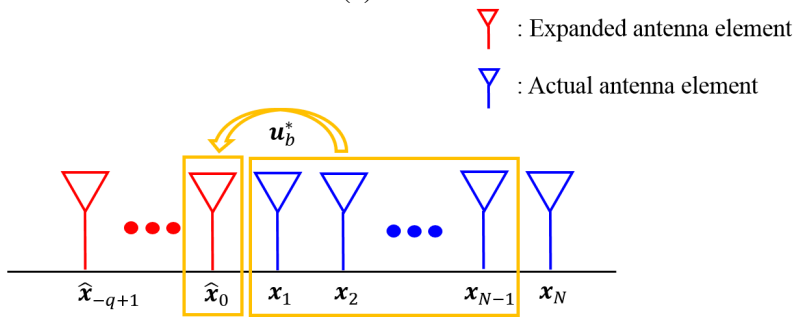
which is the process of minimizing the error between the actual received signal and the predicted received signal. In (3.9), to obtain  $\mathbf{u}_f^*$ , which minimizes the  $l_2$ -norm of the difference between  $\mathbf{x}_N$  and  $\tilde{\mathbf{x}}_N$ , I use the method of linear least squares (LLS) [68]. Since  $\mathbf{X}_f$  is not a square matrix, there is no inverse matrix. Thus,  $\mathbf{u}_f^*$  is calculated as

$$\mathbf{u}_f^* = (\mathbf{X}_f^H \mathbf{X}_f)^{-1} \mathbf{X}_f^H \mathbf{x}_N. \quad (3.10)$$

Using this transformation vector that is extracted from the original received signals, the forward linearly predicted array expansion can be conducted to extrapolate signals to the right side of the array. The transformation vector can be generated in the same way even when the number of targets is plural.



(a) forward



(b) backward

Figure 3.1: Linearly predicted expansion (a) forward (b) backward

Assuming that the antenna element is located outside and to the right of the original array antenna, its corresponding signal can be generated using transformation vector  $\mathbf{u}_f^*$  and received signals  $\mathbf{x}_2, \mathbf{x}_3, \dots, \mathbf{x}_N$ . In general, when assuming the  $(N + p)$ -th ( $p \geq 1$ ) antenna element is located outside and to the right of the original array antenna, its signal can be sequentially generated as

$$\hat{\mathbf{x}}_{N+p} = \mathbf{Y}_f^{(p)} \mathbf{u}_f^*, \quad (3.11)$$

where

$$\mathbf{Y}_f^{(p)} = \begin{cases} [\mathbf{x}_2, \mathbf{x}_3, \dots, \mathbf{x}_N] & \text{for } p = 1 \\ [\mathbf{x}_3, \mathbf{x}_4, \dots, \mathbf{x}_N, \hat{\mathbf{x}}_{N+1}] & \text{for } p = 2 \\ [\mathbf{x}_{p+1}, \dots, \mathbf{x}_N, \hat{\mathbf{x}}_{N+1}, \dots, \hat{\mathbf{x}}_{N+p-1}] & \text{for } 3 \leq p < N - 1 \\ [\mathbf{x}_N, \hat{\mathbf{x}}_{N+1}, \dots, \hat{\mathbf{x}}_{N+p-1}] & \text{for } p = N - 1 \\ [\hat{\mathbf{x}}_{p+1}, \hat{\mathbf{x}}_{p+2}, \dots, \hat{\mathbf{x}}_{N+p-1}] & \text{for } p \geq N \end{cases} . \quad (3.12)$$

Once  $\mathbf{u}_f^*$  is calculated for  $K$  time-sampled received signal vector, it can be repeatedly used to generate extrapolated signals. Within a snapshot, the linearity between the phases of the received signals are preserved, so the same transformation vector can be used to generate the expanded signals. Since the transformation vector with the smallest error is obtained using the linear least squared method, the error between the expanded signal and the real signal is also considerably small.

### 3.3.2 Backward Linearly Predicted Array Expansion

Besides the forward array expansion, I extrapolate the received signal beyond the first antenna element, as illustrated in Fig. 3.1 (b). Similar to the forward array expansion, I extract the linear relation among the  $N$  received signals. For this expansion, the relation between  $\mathbf{x}_1$  and  $\mathbf{x}_N, \mathbf{x}_{N-1}, \dots, \mathbf{x}_2$  can be expressed as the linear combination:

$$\mathbf{x}_1 \approx [\mathbf{x}_N, \mathbf{x}_{N-1}, \dots, \mathbf{x}_2] \mathbf{u}_b = \mathbf{X}_b \mathbf{u}_b = \tilde{\mathbf{x}}_1, \quad (3.13)$$

where  $\mathbf{u}_b$  is the vector composed of coefficients for the linear combination. Then, the optimal backward transformation vector  $\mathbf{u}_b^*$  can be obtained by solving the least squares problem, which is calculated as

$$\mathbf{u}_b^* = \arg \min_{\mathbf{u}_b} \|\mathbf{x}_1 - \tilde{\mathbf{x}}_1\|_2^2. \quad (3.14)$$

Similar to (3.10), I can extract the transformation vector  $\mathbf{u}_b^*$  by using the LLS method, which minimizes the norm of the difference between  $\mathbf{x}_1$  and  $\tilde{\mathbf{x}}_1$ . Thus, the solution of (3.14) is given by

$$\mathbf{u}_b^* = (\mathbf{X}_b^H \mathbf{X}_b)^{-1} \mathbf{X}_b^H \mathbf{x}_1. \quad (3.15)$$

As in the case of  $\mathbf{u}_f^*$ ,  $\mathbf{u}_b^*$  is used for the backward linearly predicted array expansion to extrapolate signals to the left side of the array.

As shown in Fig. 3.1 (b), assuming that the antenna element is located outside and to the left of the original array antenna, its corresponding signal can be generated using transformation vector  $\mathbf{u}_b^*$  and  $\mathbf{x}_{N-1}, \mathbf{x}_{N-2}, \dots, \mathbf{x}_1$ . In general, when assuming the  $(-q + 1)$ -th ( $q \geq 1$ ) antenna element is located outside and to the left of the original array antenna, its signal can be sequentially generated as

$$\hat{\mathbf{x}}_{-q+1} = \mathbf{Y}_b^{(q)} \mathbf{u}_b^*, \quad (3.16)$$

where

$$\mathbf{Y}_b^{(q)} = \begin{cases} [\mathbf{x}_{N-1}, \mathbf{x}_{N-2}, \dots, \mathbf{x}_1] \\ \text{for } q = 1 \\ [\mathbf{x}_{N-2}, \mathbf{x}_{N-3}, \dots, \mathbf{x}_1, \hat{\mathbf{x}}_0] \\ \text{for } q = 2 \\ [\mathbf{x}_{N-q}, \dots, \mathbf{x}_1, \hat{\mathbf{x}}_0, \dots, \hat{\mathbf{x}}_{-q+2}] \\ \text{for } 3 \leq q < N - 1 \\ [\mathbf{x}_1, \hat{\mathbf{x}}_0, \dots, \hat{\mathbf{x}}_{-q+2}] \\ \text{for } q = N - 1 \\ [\hat{\mathbf{x}}_{N-q}, \hat{\mathbf{x}}_{N-q-1}, \dots, \hat{\mathbf{x}}_{-q+2}] \\ \text{for } q \geq N \end{cases} . \quad (3.17)$$

In (3.17),  $\hat{\mathbf{x}}_0$  and  $\hat{\mathbf{x}}_{-q+1}$  denote the signals generated from the antenna elements located at distances  $d$  and  $qd$  to the left of the first antenna element, respectively. Similar to  $\mathbf{u}_f^*$ , once  $\mathbf{u}_b^*$  is calculated for  $K$  time-sampled received signal vector, it can be repeatedly used to generate extrapolated signals.

Finally, by using the proposed forward and backward linearly predicted array expansion, I can generate extrapolated signals  $\hat{\mathbf{x}}_{-q+1}, \dots, \hat{\mathbf{x}}_0, \hat{\mathbf{x}}_{N+1}, \dots, \hat{\mathbf{x}}_{N+p}$ . Then, the Bartlett algorithm is conducted using both the received signals by the  $N$  elements of the actual array antenna and the  $(p+q)$  generated signals, and I can achieve an improved angular resolution.

### 3.4 Simulation Results

In this section, I verify the performance of the proposed method through simulations. In our simulation, the number of antenna elements in the receiving array antenna is set

as four, which is typical in automotive radar systems [9], [54], [69]; the signal-to-noise ratio (SNR) of the received signal is set to 10 dB; the number of time sample  $K$  is set to 1361. The number of time samples is set as above to configure as the same to the actual radar system. In addition, two types of antenna spacing are used, i.e.,  $0.8\lambda$  and  $1.8\lambda$ . To prove that the proposed algorithm works well regardless of the position of the targets, the simulations were performed with varying target positions.

First, I compare the DOA estimation performance using forward, backward, and the combination of both array expansion methods to determine the direction to expand the array. By increasing the number of antenna elements in the three array expansion methods, I calculate the RMSE as

$$\text{RMSE} = \sqrt{\frac{\sum_{l=1}^L \sum_{m=1}^M \{(\theta_l - \hat{\theta}_l^{(m)})^2\}}{LM}} \text{ (}^\circ\text{)}, \quad (3.18)$$

where  $M$  denotes the number of simulation runs and  $\hat{\theta}_l^{(m)}$  denotes the estimated angular location of the  $l$ -th target in the  $m$ -th ( $m = 1, 2, \dots, M$ ) simulation. I executed  $M = 1000$  simulation runs under the same conditions. In addition, I disregarded the RMSE for the case when the number of targets was incorrectly determined.

Figure 3.2 shows the RMSE for the three variations of the proposed array expansion methods according to the number of expanded array antenna elements when two targets are randomly in the field of view with the antenna spacing of  $1.8\lambda$ . In this simulation, because the number of antenna elements is expanded to both sides when the combined forward and backward expansion is used, I calculated the RMSE at increments of two for all the variations of the proposed method. Because the angular displacement between the two targets was within the half-power beamwidth, it is difficult to resolve the two targets with the conventional Bartlett algorithm [70]. However, when the array elements are only expanded by two, the targets were distinguished. The resolution probability increases even if only two expanded antennas are added; however, because the RMSE is relatively high, it is necessary to increase the number of expanded antennas to eight or more for a more accurate angle estimation. Because

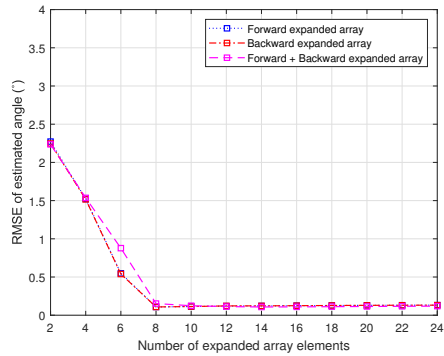
the signal generation is similar in the forward only and the backward only expansions, both methods show almost the equivalent DOA estimation performance. When the number of expanded antenna elements is less than four, little performance difference exist in the three expansion methods. After this initial evaluation, I used the combined expansion for the remainder of the simulations.

Figure 3.2 (a) also shows that the RMSE values do not decrease when the number of expanded elements is more than a certain number. This phenomenon can be related to the power of the extrapolated signal as shown in Fig. 3.3, where the power of the 4 received signals is higher than that of the extrapolated signals using forward expansion. Furthermore, the power of the extrapolated signals converges to zero as the number of expanded antenna elements increases. This can be explained as follows. Let transformation vector  $\mathbf{u}_f^*$  be expressed as

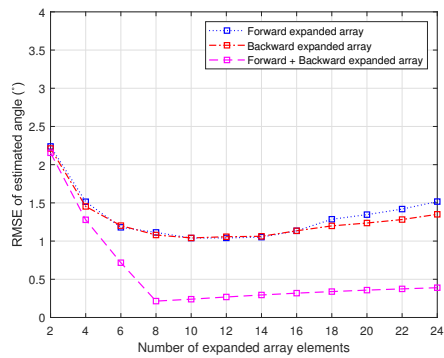
$$\mathbf{u}_f^* = [u_{f_1}^*, u_{f_2}^*, u_{f_3}^*]^T, \quad (3.19)$$

where  $u_{f_j}$  ( $j = 1, 2, 3$ ) is the  $j$ -th element in  $\mathbf{u}_f^*$ . In this simulation, because the sum of the magnitude of  $u_{f_j}$  is smaller than one, the power of the extrapolated signals gradually decreases [71]. Thus, the newly generated signals with small power cannot considerably improve the angle estimation performance, and the RMSE does not further decrease, as shown in Fig. 3.2 (a). To solve this problem, I considered the normalization of the extrapolated signals as shown in Fig. 3.2 (b). However, because the transformation vector  $\mathbf{u}_f^*$  is a vector that minimizes the error of the extrapolated signals using the linear least-squares method, if I normalize the extrapolated signals, the weight of the extrapolated signals becomes large. Because the extrapolated signals are inaccurate relative to the actual signals, the angular estimation error increases as the weight multiplied by the extrapolated signals increases.

In general, the side lobes increase when the antenna spacing is above  $0.5\lambda$ . Furthermore, when the antenna spacing is larger than  $1.0\lambda$ , undesired grating lobes are generated [50], which cannot be distinguished from the main lobe. Thus, it is difficult to estimate the angular location of the target through conventional spectral-based



(a) without normalization



(b) with normalization

Figure 3.2: RMSE according to the number of expanded antenna elements (a) without normalization and (b) with normalization

methods such as the Bartlett algorithm. If the antenna spacing is large, the angular resolution of targets is better. However, larger antenna spacing has the disadvantage that grating lobes are generated near the boresight. However, I can mitigate the side lobes and prevent the generation of grating lobes in the field of view of the array antenna, using the proposed array expansion method. Figure 3.4 shows the DOA estimation of the Bartlett algorithm with and without the proposed array expansion method for antenna spacings of  $0.8\lambda$  and  $1.8\lambda$  and 8 expanded antenna elements. Figure 3.4 (a) shows that unlike the conventional Bartlett algorithm, the algorithm including the proposed expansion distinguishes two adjacent targets. Moreover, I compare the DOA estimation performance when applying the Bartlett with the proposed method to  $0.8\lambda$  ULA antenna to when applying the conventional Bartlett to  $2.4\lambda$  ULA antenna. The angles estimated in both cases are  $(-1.9^\circ, 5.4^\circ)$  and  $(-2.2^\circ, 5.7^\circ)$ , respectively. For the ULA antenna with spacing  $2.4\lambda$ , because the half-power beamwidth is approximately  $5.44^\circ$ , the two targets can be separated; however, grating lobes appear in the range from  $-30^\circ$  to  $-15^\circ$  and from  $15^\circ$  to  $30^\circ$ . Due to these grating lobes, the angles of the targets cannot be exactly estimated. On the other hand, because the grating lobes do not appear in the field of view when using the proposed method, grating lobes cannot be confused with main lobes. Thus, these results suggest that DOA estimation and its angular resolution can be improved using the proposed method, even when the antenna spacing is smaller than  $1.0\lambda$ . Similar trends can be appreciated when considering a spacing of  $1.8\lambda$ , and grating lobes appear when using a spacing of  $5.4\lambda$ , as shown in Fig. 3.4 (b).

Next, I compare the performance of the proposed method with that of the conventional interpolation using LLS method [54]. Figure 3.5 (a) shows the DOA estimation of the Bartlett algorithm with and without the proposed method, and that of the Bartlett algorithm using the conventional LLS method. For the conventional LLS method [54], sector  $\Theta = [\theta_L, \theta_R] = \{\theta \mid \theta_L \leq \theta \leq \theta_R\}$  must be set, which indicates the observation interval in the field of view of the array antenna. In this simulation, the sector

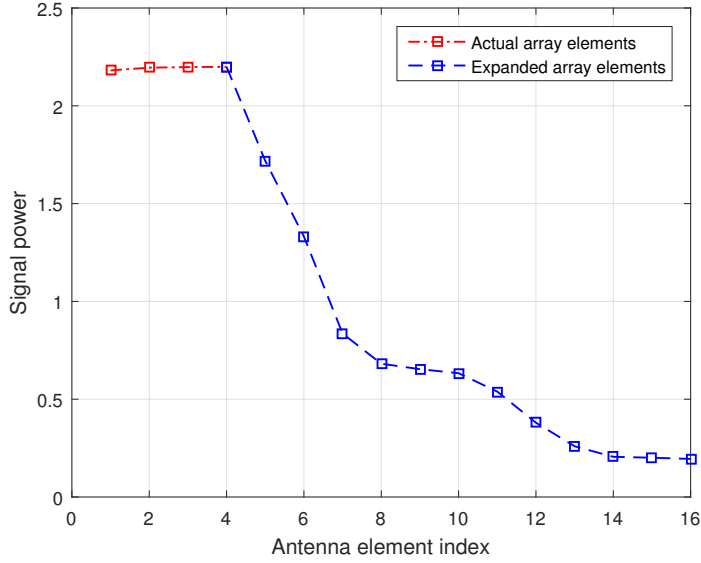
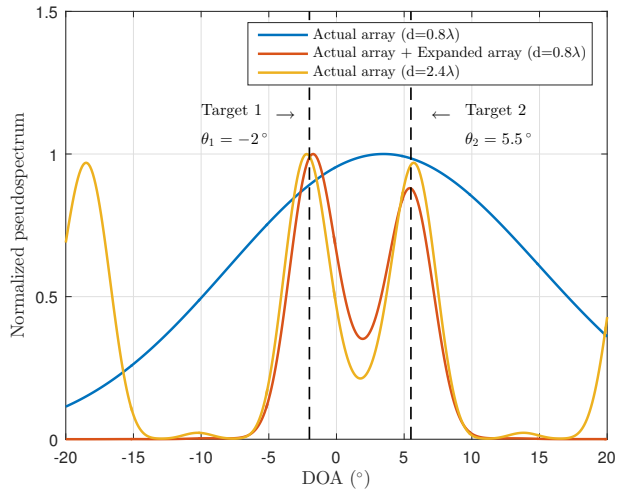
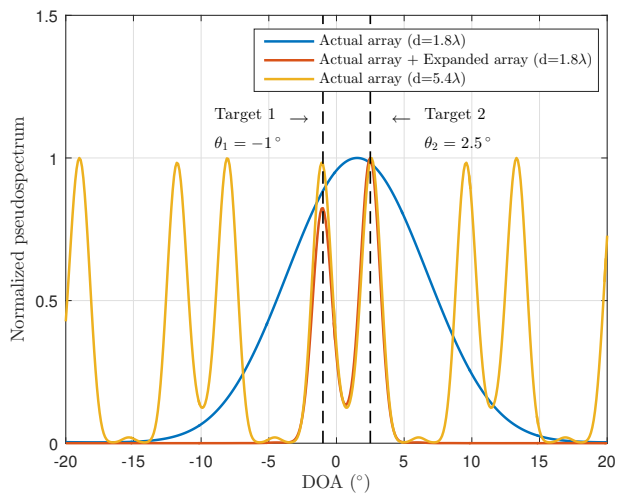


Figure 3.3: Power of the actual (1 to 4) and extrapolated (5 to 16) signals

of the conventional LLS method is given as  $[-15^\circ, 15^\circ]$  with 8 expanded antenna elements. As shown in Fig. 3.5 (a), regardless of the range of the sector, the proposed method has better angle estimation accuracy than the conventional LLS method. In Fig 3.5 (b), when the sector is  $[-15^\circ, 15^\circ]$ , the angular location of the targets using conventional LLS method cannot be distinguished, and only one target is estimated at  $1.1^\circ$ . In this case, no apparent performance difference exists compared to the conventional Bartlett algorithm. However, when using the proposed method, the angular locations of the targets are accurately estimated at  $-0.9^\circ$  and  $2.9^\circ$ . In the conventional LLS method, when the range of the sector is close to the range of target angles, the accuracy of the estimation is improved. Thus, I use more narrow sector as  $[-5^\circ, 5^\circ]$ , and the estimation results are also given in Fig. 3.5 (b). When the range of the sector gets narrow, the angles of the targets are estimated as  $-1.7^\circ$  and  $1.8^\circ$ , which are close to actual angles; however, even when the narrow range of the sector is used, the estimation error is larger than that of using the proposed method. In addition, if the target exists outside the sector, the conventional LLS method cannot accurately estimate the

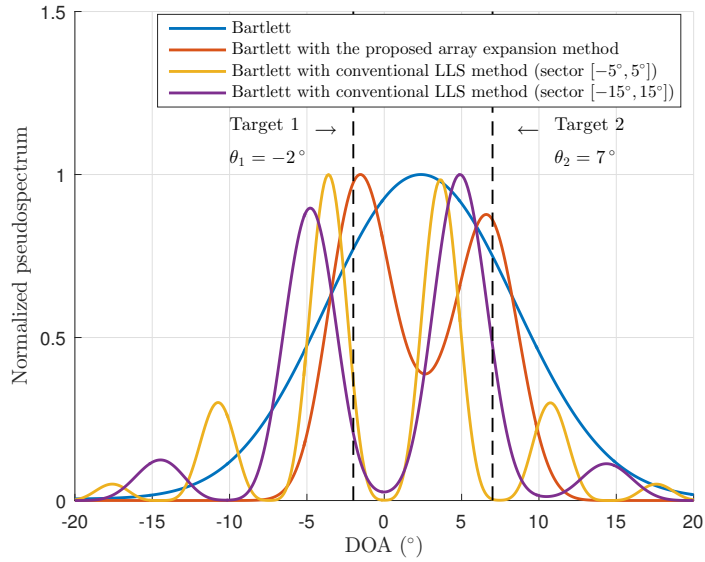


(a)  $0.8\lambda$

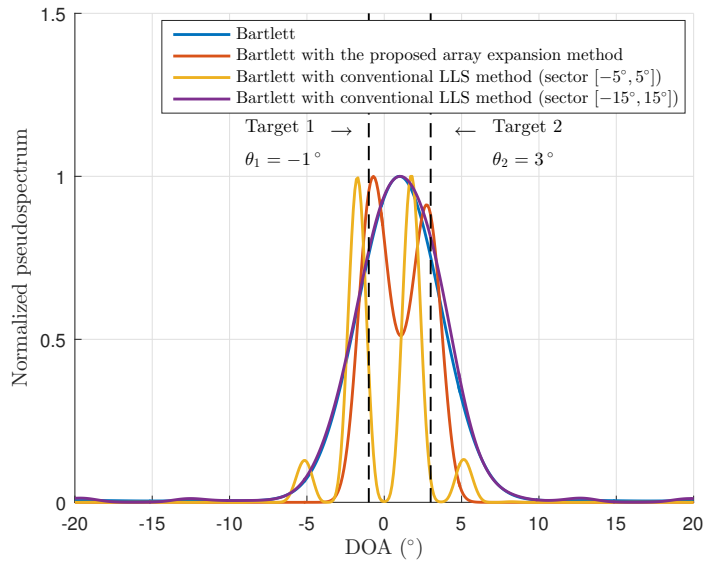


(b)  $1.8\lambda$

Figure 3.4: DOA estimation of the Bartlett algorithm with and without the proposed array expansion method for spacing of (a)  $0.8\lambda$  and (b)  $1.8\lambda$



(a)  $0.8\lambda$



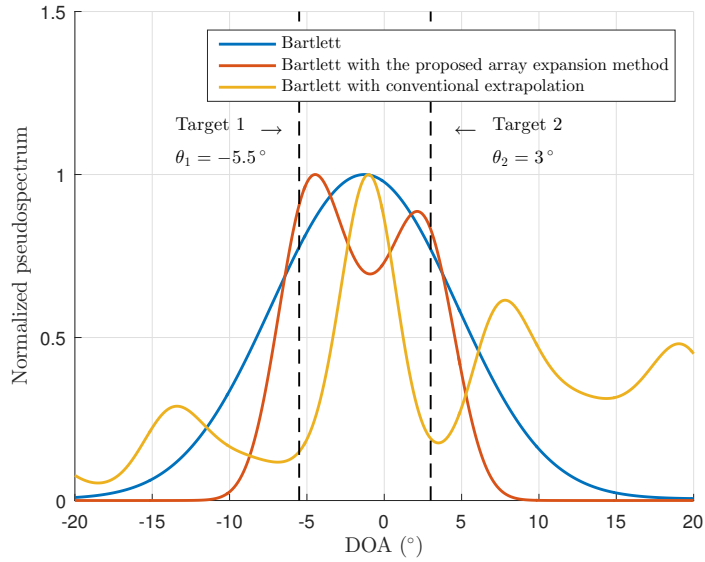
(b)  $1.8\lambda$

Figure 3.5: DOA estimation of the Bartlett algorithm with and without the proposed array expansion method, and it using the conventional LLS method for spacing of (a)  $0.8\lambda$  and (b)  $1.8\lambda$

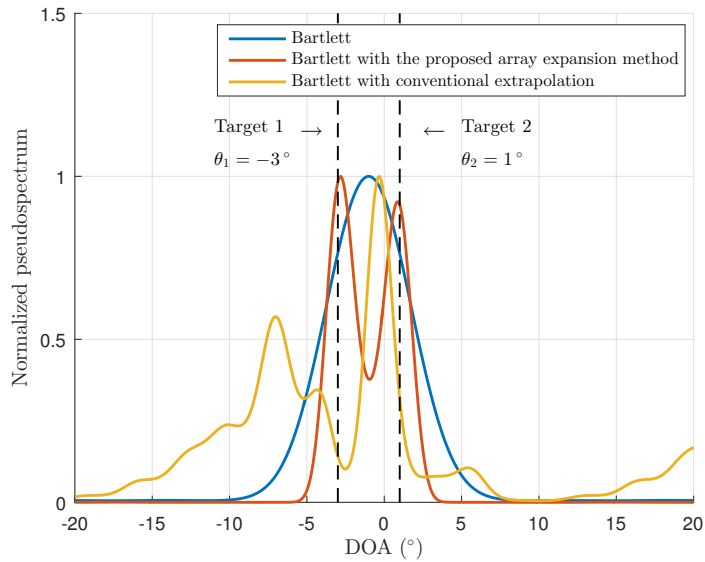
position of the target [53]–[55]. Overall, the proposed method outperforms conventional LLS method in estimation accuracy and angular resolution without requiring to define a sector and regardless of antenna spacing.

Then, I compare the DOA estimation using the proposed method with that of using conventional extrapolation [57], [58]. In the conventional extrapolation, a transformation vector is obtained by using an autocorrelation matrix of the received signal, and the number of antenna elements can be expanded at each side only by the same number of the actual antenna elements [57]. Therefore, I considered 8 expanded antenna elements. Figures 3.6 (a) and 3.6 (b) show the DOA estimation of the Bartlett algorithm using the proposed array expansion and conventional extrapolation for spacing of  $0.8\lambda$  and  $1.8\lambda$ , respectively. When the proposed method is applied, the two targets are completely separated, and the estimated angles are  $-4.8^\circ$  and  $2.2^\circ$  for  $0.8\lambda$ . On the other hand, when using conventional extrapolation, the exact angular locations of the targets cannot be estimated because four peak values appear in the pseudospectrum. Even when the antenna spacing is larger, as shown in Fig. 3.6 (b), the proposed method clearly outperforms the conventional extrapolation.

I also evaluate the performance of the proposed method and conventional extrapolation by varying the number of expanded antenna elements. Figures 3.7 and 3.8 show the RMSE and resolution probability according to the number of expanded antenna elements, respectively. The resolution probability is defined as the rate of successfully separated targets over the simulations, where the angular spacing of two targets is  $4^\circ$  with antenna spacing of  $1.8\lambda$ . For both methods, when the number of expanded antenna elements is below 4, the two targets are mostly indistinguishable as shown in Fig. 3.8. However, for increased number of expanded antenna elements, the angle estimation accuracy tends to improve. The best performance of conventional extrapolation is achieved when the number of expanded antenna elements is approximately twice the number of the actual antenna elements. However, the performance of the proposed method has more improvement when the number of antenna elements is more than two



(a)  $0.8\lambda$



(b)  $1.8\lambda$

Figure 3.6: DOA estimation of the Bartlett algorithm with and without the proposed array expansion method, and it using conventional extrapolation for spacing of (a)  $0.8\lambda$  (b)  $1.8\lambda$

times of the number of actual antenna elements. Moreover, the proposed method has a lower computational complexity than the conventional extrapolation, which requires the calculation of the transformation vector whenever signals are generated [57], [58]. In the process of creating an expanded array, an expanded signal is first generated using the actual received signal. However, if more than  $2N$  expanded antennas are generated, only the expanded signal will be used to generate the new expanded signal, so the accuracy of the expanded signal will be lowered. However, since the proposed method generates an expanded signal with fairly high accuracy, the angle estimation performance is improved even if the number of antennas is increased to  $3N$ . Although the optimal number of the expanded antennas varies depending on the position of the target, basically,  $2N$  is most appropriate to generate, and if SNR is very high, performance increases even when  $3N$  expanded signals are generated.

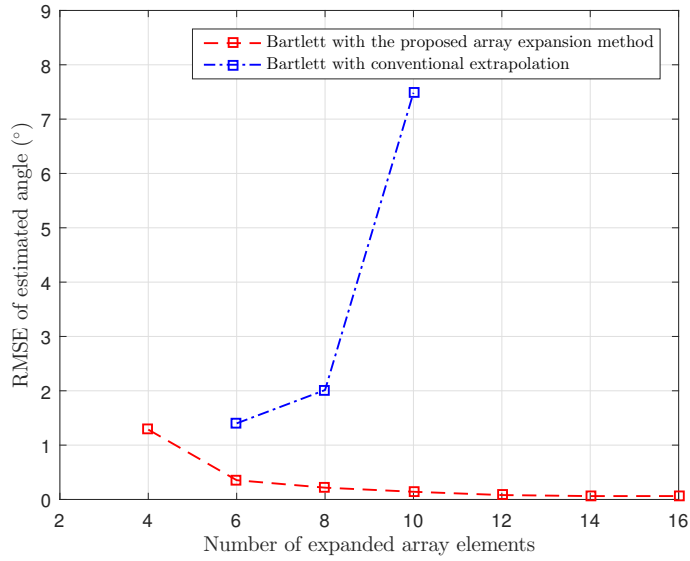


Figure 3.7: RMSE according to the number of antenna elements using the proposed method and conventional extrapolation

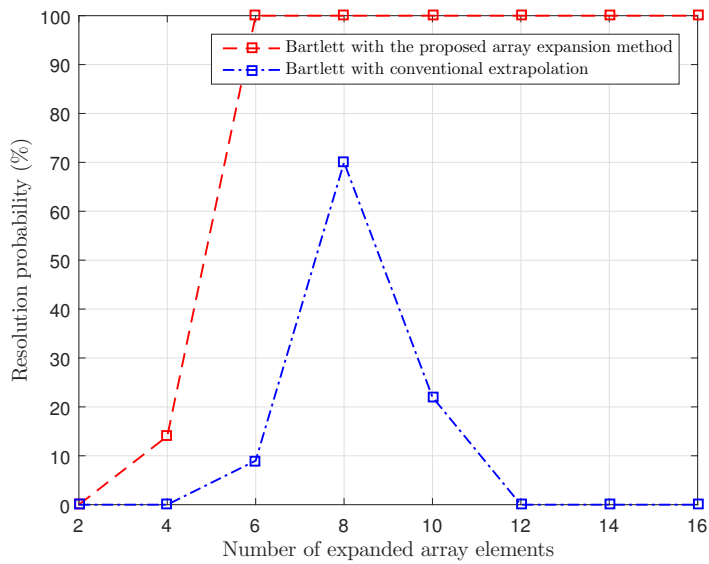


Figure 3.8: Resolution probability according to the number of antenna elements using the proposed method and conventional extrapolation

Figure 3.9 shows how RMSE varies with the number of targets. Even though the number of targets is the same, the accuracy varies depending on the position of the target. As the number of targets increases, the angle estimation accuracy decreases. Furthermore, the conventional extrapolation method cannot accurately estimate the number of targets when the number of targets is more than 3, but the proposed method is quite accurate even if the number of targets increases. Figure 3.10 shows how RMSE varies with the number of snapshots. The SNR was 0 dB, the DOAs of targets were set to  $-2^\circ$  and  $4^\circ$ , respectively, and 10000 simulations were performed. When multiple snapshots are used, the accuracy of the used data to find DOAs of targets can be increased, so the angle estimation performance is improved. In Fig. 3.10, as the number of snapshots used increases, the RMSE of estimated angle is decreased for both algorithms. Figures 3.11 and 3.12 show how the angular resolution and RMSE vary with SNR. The performance of the proposed method and the conventional LLS method are compared. To compare the performance under the same conditions as the conventional method, the number of extrapolated antennas was set to 8. The SNR was increased by 1 dB, and 10000 simulations were performed for each. The DOAs of targets were randomly set in the field of view. The performance of the proposed method is slightly degraded when the SNR is very low, but otherwise, the performance is much improved than that of the conventional LLS method.

To investigate the improvement of the proposed array expansion method compared to the angular resolution of various NLAs proposed previously, I simulated the resolution probability by increasing the angular interval between the targets by  $0.1^\circ$ . The total antenna aperture size is set to  $11\lambda$  and 6 antennas are used. Figure 3.13 shows how the angular resolution varies with the antenna array type for the two SNRs. In Fig. 3.13 (a), when the SNR is 10dB, the angular resolution is improved by more than  $2^\circ$  compared to other NLAs. However, because the proposed method is sensitive to SNR changes, the angular resolution of the proposed method approaches that of conventional NLAs under low SNR conditions in Fig. 3.13 (b). Moreover, in Fig. 3.14, the

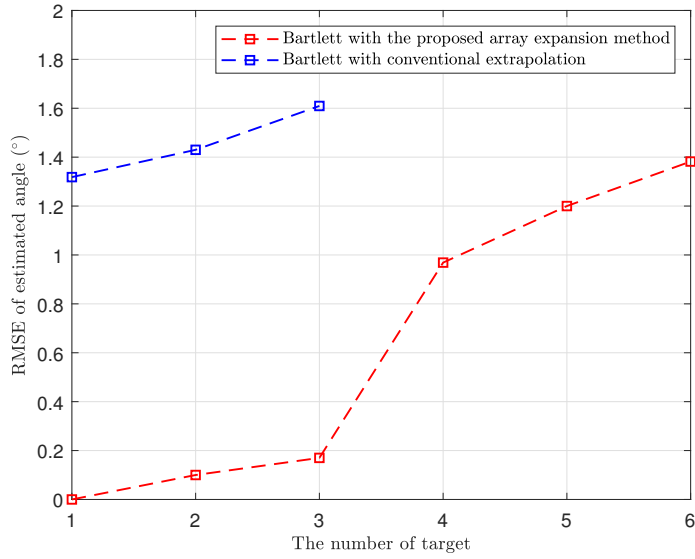


Figure 3.9: RMSE according to the number of targets using the proposed method and conventional extrapolation

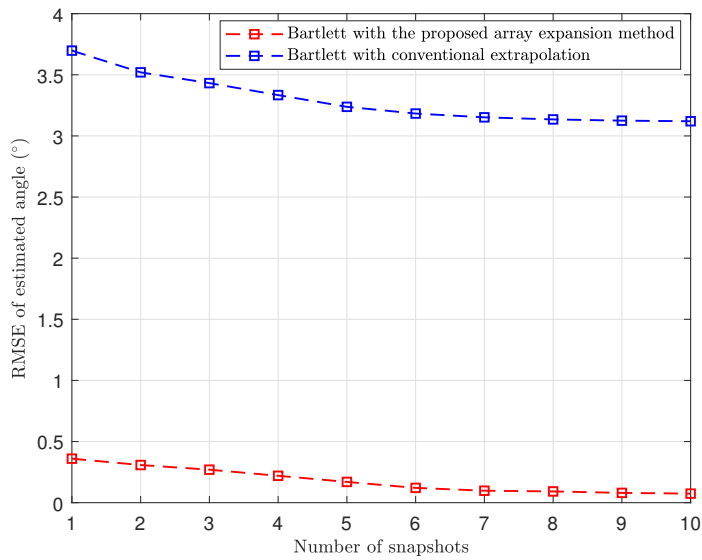


Figure 3.10: RMSE according to the number of snapshot using the proposed method and conventional extrapolation

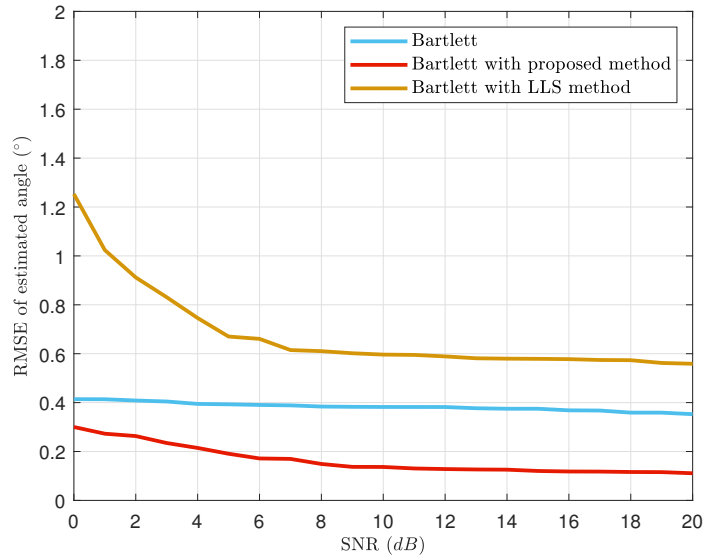


Figure 3.11: RMSE according to SNR using the proposed method and conventional LLS method

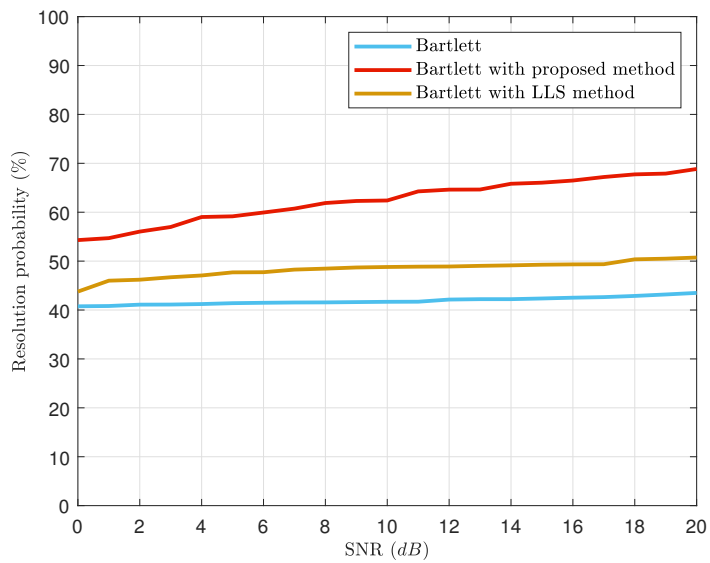
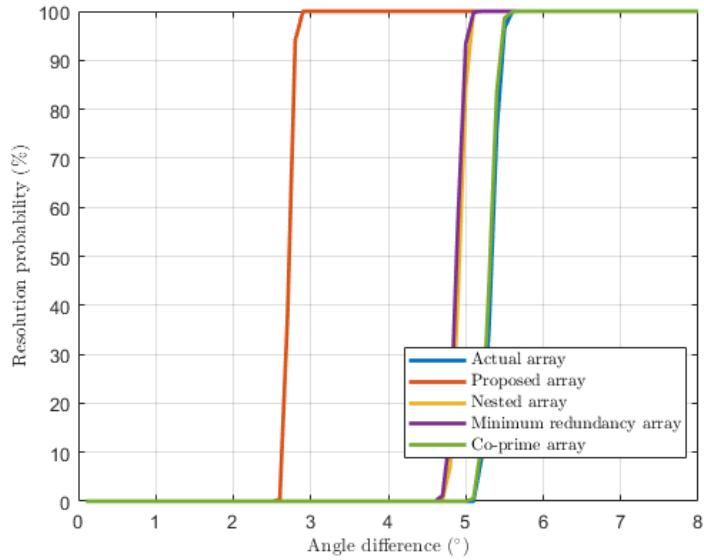


Figure 3.12: Resolution probability according to SNR using the proposed method and conventional LLS method

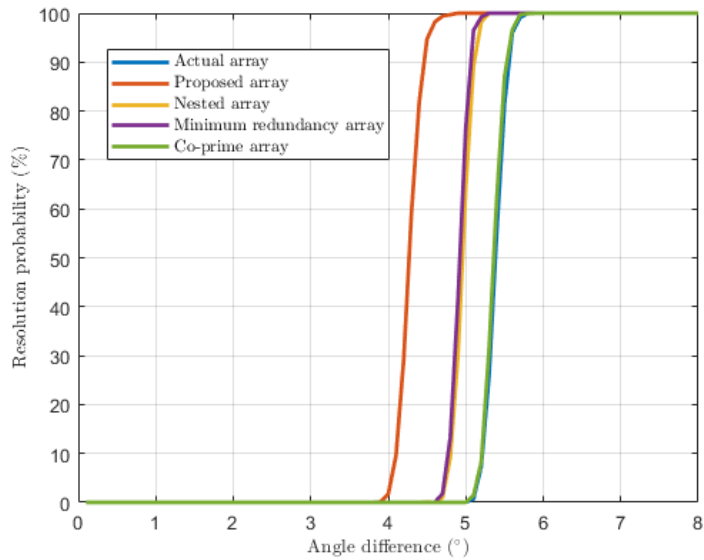
additional simulations were performed in the presence of five targets in order to check whether the proposed method is applicable even in the presence of a large number of targets. When multiple targets are in close proximity and the targets are detected using the conventional NLAs, it appears that there are three or four targets because not all targets can be distinguished. However, all targets are correctly detected by using the proposed array expansion method.

In addition, I applied the proposed array expansion to the MUSIC DOA estimation algorithm, which delivers a high resolution and is reported to outperform the conventional Bartlett algorithm [67]. MUSIC algorithm is one of the subspace based algorithms. MUSIC is a method of estimating the DOA of the target using the orthogonality between the received signal and the noise component. After eigenvalue decomposition of the covariance matrix of the received signal, the eigenvector corresponding to the noise component is multiplied by the steering vector to find the DOAs of the targets. However, to find the DOAs of targets using the MUSIC algorithm, the number of targets should be estimated in advance.

The MUSIC angle estimation algorithm is performed assuming that the targets correspond to the most dominant eigenvalues obtained through the eigenvalue decomposition of the covariance matrix of the received signal. Therefore, if the number of estimated targets is more than the number of actual targets, the noise component that corresponds to a large eigenvalue can be recognized as a target. Conversely, if the number of estimated targets is less than the number of actual targets, the signal component that corresponds to a small eigenvalue can be recognized as noise. Thus, in the MUSIC algorithm, the difference between the estimated and actual number of targets undermines the algorithm performance [69]. Figure 3.15 shows the DOA estimation of the MUSIC algorithm with and without the proposed array expansion method for two targets located at  $-1^\circ$  and  $2.5^\circ$ , respectively with the antenna spacing of  $1.8\lambda$ . In addition, I tested the algorithm considering estimated number of targets  $\hat{L} = 2$  and  $\hat{L} = 3$ , to evaluate the effect of an erroneous number of targets in the latter case (i.e.,



(a)  $SNR = 10dB$



(b)  $SNR = -5dB$

Figure 3.13: Resolution probability according to the DOA difference using the actual array, proposed array, minimum redundancy array, nested array, co-prime array, when SNR is (a) 10dB (b) -5dB

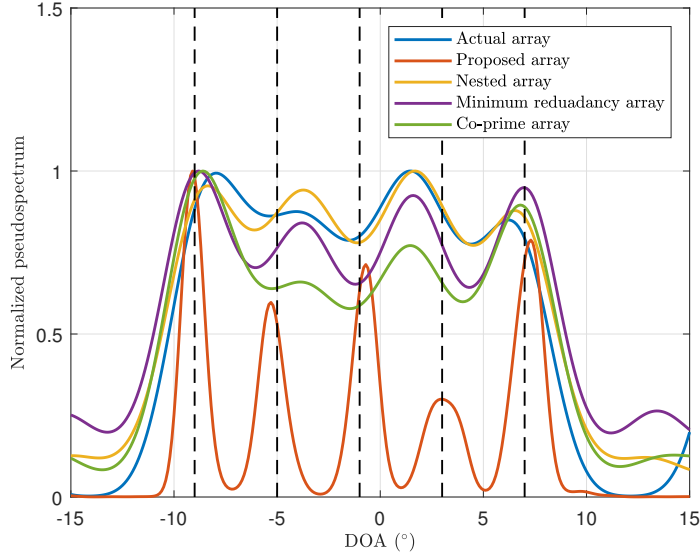


Figure 3.14: Normalized Bartlett pseudospectra of different antenna arrays

$\hat{L} = 3$ ). As shown in the figure, when  $\hat{L} = 3$ , the two targets cannot be identified by the MUSIC algorithm. However, when the proposed method is applied, the angular locations of the targets can be correctly found regardless of the estimated number of targets. Furthermore, for statistical analysis, I analyzed the RMSE and resolution probability through 10,000 simulations. RMSE is calculated using the equation in (3.18). The resolution probability is calculated from the number of times that the targets were properly separated into two targets during a total of 10,000 tests. As shown in Table 3.1, when the proposed method is applied, the two targets are completely separated. In addition, although the MUSIC algorithm cannot detect the targets correctly if the number of targets is not known in advance, the resolution probability is increased by 20% or more when the proposed method is applied. This is almost the same as when the conventional MUSIC algorithm is applied when the number of targets is known. The RMSE is also lowered, which considerably improves the angle estimation accuracy.

In addition, I verified whether the proposed array expansion method can be applied when more than two targets exist. Hence, Table 3.2 shows a comparison among

Table 3.1: RMSE and resolution probability of MUSIC DOA estimation methods for two targets

DOA estimation method	RMSE ( $^{\circ}$ )	Resolution probability (%)
MUSIC ( $\hat{L} = 2$ )	0.22	92.37
MUSIC with the proposed method ( $\hat{L} = 2$ )	0.13	100
MUSIC ( $\hat{L} = 3$ )	0.34	68.23
MUSIC with the proposed method ( $\hat{L} = 3$ )	0.27	91.58

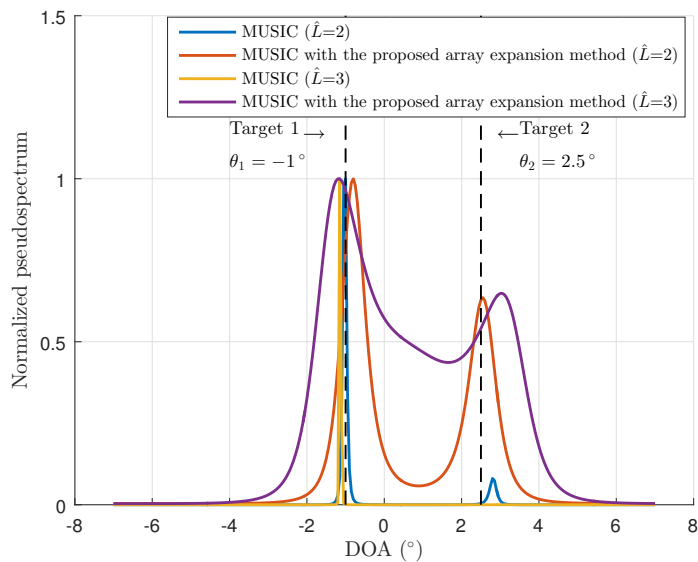


Figure 3.15: DOA estimation of the MUSIC algorithm with and without the proposed array expansion method considering correctly estimated ( $\hat{L} = 2$ ) and incorrectly estimated ( $\hat{L} = 3$ ) number of targets

the Bartlett and MUSIC algorithms, with and without the proposed array expansion method, the Bartlett with the conventional LLS method, and the Bartlett with the conventional extrapolation for three targets located at  $-8^\circ$ ,  $-1^\circ$ , and  $7^\circ$ , and correct the estimation for  $\hat{L} = 3$  of the number of targets for the MUSIC algorithm. As shown in Table 3.2, the three targets cannot be distinguished using both the conventional Bartlett algorithm and the Bartlett algorithm with the conventional extrapolation method. However, the three targets are successfully decomposed using the proposed array expansion method. Moreover, applying the proposed method to the MUSIC algorithm shows that the RMSE is slightly higher but the separation probability is higher than that of the conventional MUSIC algorithm. The proposed array expansion method is not suitable for MUSIC algorithm in low SNR environment. Therefore, I confirmed that the proposed method can achieve more performance improvement when applied to the Bartlett algorithm than the MUSIC algorithm. In the simulation results, the DOA estimation using the Bartlett algorithm with the proposed method obtains angles closer to the actual values. Furthermore, because the computational complexity of the Bartlett algorithm is much lower than that of the MUSIC algorithm, which relies on the eigenvalue decomposition [69], the former with the proposed array expansion method can be considered as the most suitable DOA estimation method for automotive radar systems.

### **3.5 Experimental Results**

This section presents the performance of the proposed method from the experiments with an actual automotive radar system. I conducted the experiments in a test field using a long-range radar manufactured by Mando Corporation (Republic of Korea). This system has a field of view from  $-10^\circ$  to  $10^\circ$  and maximum detection range of 200 m. In addition, the number of transmitting and receiving antenna elements are 1 and 4, and the antenna spacing between receiving antenna elements is  $1.8\lambda$ . Moreover,

Table 3.2: RMSE and resolution probability of various DOA estimation methods for three targets

DOA estimation method	RMSE ( $^{\circ}$ )	Resolution probability (%)
Bartlett algorithm	-	0
Bartlett with the proposed method	0.27	100
Bartlett with conventional LLS method	1.03	47.94
Bartlett with conventional extrapolation	-	0
MUSIC ( $\hat{L} = 3$ )	0.69	88.59
MUSIC with the proposed method ( $\hat{L} = 3$ )	0.97	93.06

the system transmits a 76.5 GHz frequency-modulated continuous wave radar signal with bandwidth of 500 MHz and 10 ms sweep time for the up- and down-chirp signals. The transmitted signal is multiplied by signals reflected from targets, and the multiplied signal passes through a low-pass filter. The proposed array expansion method is applied to the time-domain low-pass filtered output.

In the experimental scenario, I placed only two target vehicles in the field of view of the radar system to mitigate the effects of other external factors and analyze only the signals reflected from them, as shown in Fig. 3.16. Two identical target vehicles are placed at the same distance but at different angles. Two vehicles are placed 30 m away from the radar-equipped vehicle, and 4.8 m apart from the center of each vehicle. In addition, they are located at  $-4^{\circ}$  and  $4^{\circ}$  in the direction that the radar-equipped vehicle is looking at. For the measured signals in this environment, the normalized pseudospectrums of the Bartlett algorithm with and without the proposed array expansion method, and the Bartlett algorithm with conventional LLS method and conventional extrapolation are shown in Fig. 3.17. Similar to the simulation results, the Bartlett algorithm by itself was unable to distinguish the two targets and they were recognized as a single target. By applying the proposed method, the two targets were identified, and



Figure 3.16: Experimental setup with two targets located in front of a radar-equipped vehicle

their angular positions accurately estimated at  $-5.3^\circ$  and  $5.8^\circ$ . Even though a narrow sector including the two target vehicles was set when using conventional LLS method as  $[-15^\circ 15^\circ]$ , the estimated values were highly inaccurate. Moreover, the Bartlett algorithm with conventional extrapolation showed poor and unreliable identification and angle estimation results.

To quantify the performance of the proposed method in the statistical aspect, I evaluated the received signals from 298 measurements considering the same experimental conditions and calculated the RMSE and resolution probability for the different methods, as listed in Table 3.3. The comparison includes the Bartlett algorithm, as well as the algorithm with the proposed array expansion method, conventional LLS method, and conventional extrapolation. The Bartlett algorithm by itself was unable to identify the two targets from any of the 298 signals (i.e., resolution probability of 0%), and thus, the RMSE was not calculated. The Bartlett algorithm with either conven-

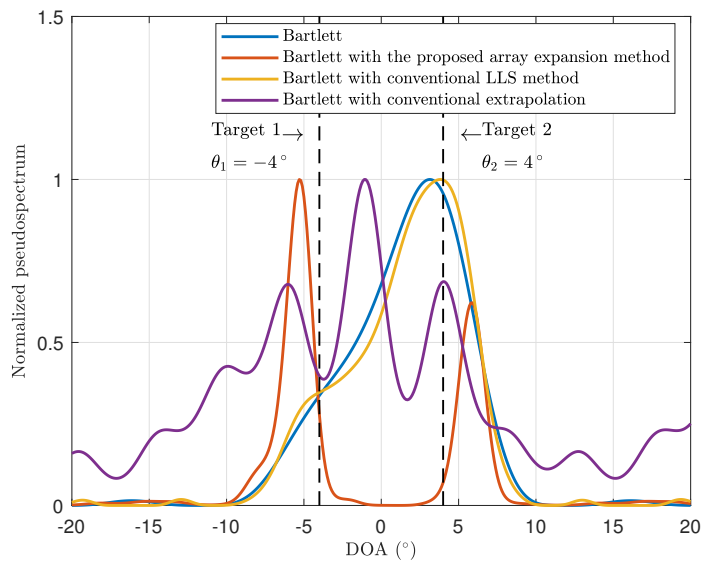


Figure 3.17: DOA estimation of the conventional Bartlett algorithm with and without the proposed array expansion method, and it using conventional LLS method and conventional extrapolation

Table 3.3: RMSE and resolution probability of various DOA estimation methods in actual experiments

DOA estimation method	RMSE ( $^{\circ}$ )	Resolution probability (%)
Bartlett algorithm	-	0
Proposed method	1.59	99.33
Conventional LLS method	1.69	42.95
Conventional extrapolation	3.22	17.45

tional LLS method or conventional extrapolation poorly identified the two targets, and the estimation accuracy was low. However, the Bartlett algorithm with the proposed method showed the best performance with the highest resolution probability and the lowest RMSE among the compared methods. Moreover, in the proposed method, I can increase the number of array elements further in contrast to the conventional extrapolation. In this case, the two targets are separated by more than 99% resolution probability.

### 3.6 Computational complexity

The computational complexity of the Bartlett algorithm is about  $O(P(2N - 1)(N + P))$ .  $P$  denotes the sampling grid of angle. The computational complexity of conventional MUSIC algorithm is about  $O(N^3 + JNL)$  to proceed eigenvalue decomposition.  $J$  is the samples of the MUSIC null-spectrum function. In the proposed algorithm, the computational complexity depends on how many expanded antennas are generated. Assuming that the number of expanded antennas is  $2N$ , the computational complexity is approximately  $O((18P + 4K)N^2)$ . Furthermore, I measured the actual algorithm execution time. When the execution time of the Bartlett algorithm is 1, the execution time of the proposed method with Bartlett algorithm is 1.3 and the MUSIC algorithm is 1.8. Compared to the conventional Bartlett algorithm, the computational complexity

is slightly increased, but the computational complexity is still lower than that of the MUSIC algorithm.

### **3.7 Conclusion**

In this chapter, I proposed an improved DOA estimation method using linearly predicted array expansion for automotive radar systems having a small number of antenna elements. The performance of the proposed method was verified by simulations and actual experiments. In particular, I tested the proposed method using the Bartlett and MUSIC algorithms, which are widely applied in automotive radar systems. Unlike conventional LLS method, the proposed method does not require a predefined sector. Furthermore, the proposed method has a low computational complexity than conventional extrapolation which requires the repeated calculation of transformation vectors to generate extrapolated signals. Overall, the proposed method outperforms the other approaches in every simulation and experiment with respect to estimation accuracy and angular resolution. Therefore, the proposed method could improve the low angular resolution caused by a small number of antenna elements. I expect that the proposed method will be an efficient and simple approach to improve DOA estimation without requiring additional hardware for automotive radar systems.

## **Chapter 4**

# **Improved DOA Estimation Method by Distinction of Different Transmit Signals in Automotive MIMO FMCW Radar Systems**

### **4.1 Introduction**

There are several types of automotive radar systems. Among them, FMCW is widely used because of the low complexity of the received signal processing procedure [72]. The FMCW modulation uses ramp signals, and the duration of the entire ramp signal determines the velocity resolution [15]. In recent years, a modified version of the FMCW modulation has gained interest; in this method, a fast-ramp signal uses multiple linear frequency modulated signals consecutively in a short time span. In the fast-ramp modulation, a two-dimensional fast fourier transform (2D-FFT) is used to estimate velocity and range of a target [17], [18].

To enhance the angular resolution of automotive radar systems, the need for MIMO radar systems is on the rise [73]–[75]. The MIMO radar systems improve target detection, recognition, and tracking performance [76]–[78]. In MIMO radar systems, estimating the DOAs of targets using a small number of antennas is possible because virtual antennas are generated by the relative position of the transmitting and receiv-

ing antennas [79]–[81]. However, if every antenna transmits the same signal simultaneously, the signals cannot be distinguished at the receiver. To solve this problem, various techniques have been proposed for distinguishing signals [82], [83].

One method is time division multiplexing (TDM). In the TDM method, each transmitter radiates signals at predetermined time intervals. The signals are radiated sequentially from each transmit antenna element. However, in this method, using more transmit antennas decreases the power that can be transmitted in each time slot. In addition, the period of the entire chirp is increased, and the detectable maximum velocity is reduced due to the velocity ambiguity. This negates the advantages of a MIMO radar system. To overcome the disadvantage of the TDM MIMO radar system, binary phase modulation (BPM) MIMO wherein, each transmitter simultaneously radiates signals that are coded differently from each other can be used [82]. Using this modulation has the advantage that more power can be used in one time slot than the TDM because it can radiate signals simultaneously from different transmit antennas. However, this modulation method also needs to be divided into odd and even chirps in the decoding process, and the maximum detectable velocity is reduced by half, as in the TDM method. In addition, computational complexity is high because the time domain signal is used in the signal distinction process.

In this chapter, I propose an advanced signal distinction method for automotive MIMO fast-ramp radar systems. First, I use space-time block codes [84], [85] to distinguish the transmitted signals. Space-time block codes are used to generate different transmit signals that have orthogonal properties, and the phases of the transmit signals are shifted at regular intervals depending on the number of transmit antennas. Then, to find the appropriate array for DOA estimation, I match each of the distinguished transmitted signals to their transmit antenna by applying the DML algorithm. By identifying the signal that is radiated from the first transmit antenna, the maximum detectable velocity is not reduced, and the DOA estimation accuracy is enhanced. If the transmitted signals are mismatched, the correlation between the received signal and the steering

matrix is reduced, and DOA estimation performance is degraded. Since DML estimates the method by projecting the received signal vectors onto the nullspace of the steering matrix, it can be used to distinguish the transmitted signals resulting from different transmit antennas. Compared to the conventional BPM MIMO method, different signals can be distinguished through simple signal processing.

The remainder of this chapter is organized as follows. First, the fundamentals of a fast-ramp FMCW radar system, coded MIMO radar signal, and deterministic maximum likelihood are introduced in Section 4.2. In Section 4.3, a method of classifying different transmitted signals using DML is presented. Then, the DOA estimation performance using simulations and experimental results are analyzed in Section 4.4. Finally, the conclusions are provided in Section 4.5.

## 4.2 Fundamentals of fast-ramp FMCW radar system and DML DOA estimation algorithm

### 4.2.1 Fundamentals of fast-ramp FMCW radar system

I consider a fast-ramp FMCW radar system. The received signal in a fast-ramp FMCW radar system can be expressed as follows:

$$s_{2D}[n, l] = \sum_{l=0}^{L-1} e^{j2\pi\left(\frac{2f_c \cdot v}{c} + \frac{2B \cdot (R+v \cdot T_{RI} \cdot l)}{T_{sw} c}\right) \cdot n \cdot T_s} \cdot e^{j2\pi \cdot \frac{2f_c \cdot (R+v \cdot T_{RI} \cdot l)}{c}} \cdot \text{rect}\left(\frac{t - l \cdot T_{RI}}{T_{sw}}\right), \quad (4.1)$$

where  $s_{2D}[n, l]$  is the 2D time-domain received signal,  $n$  is the time sample index,  $l$  is the chirp index,  $L$  is the total number of chirps and  $f_c$  is the carrier frequency of the transmitted signal. In addition,  $R$  is the distance to the target,  $v$  is the relative velocity between the target and the sensor,  $c$  is the speed of light,  $B$  is the sweep bandwidth of the transmitted signal,  $T_{RI}$  is the repetition interval between each chirp,  $T_{sw}$  is the sweep time of the up-chirp transmitted signal,  $T_s$  is the sampling interval, and  $\text{rect}(\cdot)$

is a rectangular pulse. The 2D-FFT result of  $s_{2D}$  can be expressed as:

$$S_{2D}(p, q) = \sum_{l=0}^{L-1} \sum_{n=0}^{N_s-1} e^{j \cdot 4\pi f_c \cdot R/c} \cdot e^{j \cdot 4\pi \frac{v \cdot T_{RI} \cdot f_c}{c} \cdot l} \cdot e^{j \cdot 2\pi \left( \frac{2f_c \cdot v}{c} + \frac{2B \cdot R}{T_{sw} c} \right) \cdot n \cdot T_s} \cdot e^{-j \cdot 2\pi \left( \frac{l \cdot q}{L} + \frac{n \cdot p}{N_s} \right)}, \quad (4.2)$$

where  $p = \left( \frac{2f_c \cdot v}{c} + \frac{2B \cdot R}{T_{sw} c} \right) T_s \cdot N_M$ ,  $q = \frac{2v \cdot f_c \cdot T_{RI} \cdot L_M}{c} = f_d T_{RI} L_M$ . In addition,  $N_M, L_M$  is the matrix size of  $S_{2D}$  after zero padding,  $f_d$  is the doppler frequency of a target, and  $N_s$  is the total number of time samples in a chirp.

#### 4.2.2 Coded MIMO radar signal

In MIMO radar systems, orthogonal waveforms are used to distinguish the  $N_t$  different transmitted signals. First, assuming two transmit antennas without loss of generality, one of the simple methods to accomplish orthogonality is to use space-time block code. This method generates two signals with orthogonal properties by using a binary code.

$$\mathbf{C} = \begin{bmatrix} c_1 & c_2 \\ -c_2^* & c_1^* \end{bmatrix}, \quad (4.3)$$

where  $\mathbf{C}$  denotes the coding matrix and  $[\cdot]^*$  denotes the complex conjugate operator. Because automotive radars use fast-ramp modulation, the space-time block code is applied to fast-ramp modulation to generate several orthogonal signals. The fast-ramp modulation method uses many chirps rapidly in one snapshot. Then, signal processing is conducted by using sequentially received chirps. In this study, I used  $N_t$  kinds of transmit signals. If two transmit antennas are used, one is the same signal which is represented in (4.1). To distinguish the two transmitted signals, another signal, whose phase is shifted by  $\pi$  for every even numbered chirp is used. Figure 4.1 represents the two different transmitted signals.  $s_1$  denotes the same signal as the one chirp of  $s_{2D}$  in (4.1) and  $s_2$  denotes the phase shifted signal by  $\pi$ . Each transmitted signal

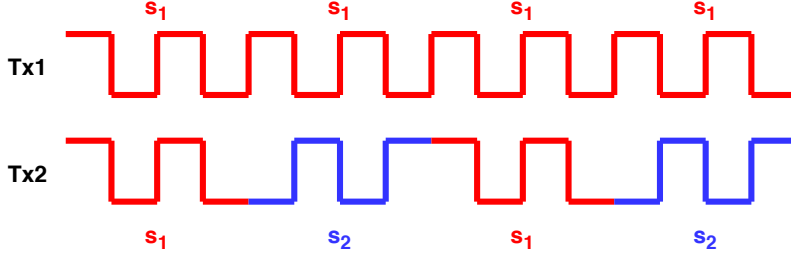


Figure 4.1: Transmitted signals from two different transmit antennas

represents four chirps in Fig. 4.1. The signal radiated from Tx2 changes the phase by  $\pi$  for every even chirp. Thus, the two signals are orthogonal to each other. Similarly, if  $N_t$  transmit antennas are used, different  $N_t$  orthogonal signals are transmitted using Hadamard code [86].

### 4.2.3 Deterministic maximum likelihood

DML is an algorithm which can be used to find the DOA of a target. The DOA estimation algorithm is divided into two main approaches depending on the angle estimation method. One is a spectral approach and the other is a parametric approach. A spectral approach is a way to make the location of a target appear in a spectral form [67]. The parametric approach is a method of estimating the DOA by searching the values of the parameters related to the DOA. DML is one of the DOA estimation algorithms corresponding to the parametric approach. DML estimates the DOA by projecting received signal vectors onto the null space of the steering matrix. It results in concentrating on the phase information of the received signal. First, I assume that the received signal  $\mathbf{x}(k)$  is a temporally white Gaussian random process, with covariance matrix  $\sigma^2\mathbf{I}$ . If  $G$  targets exist, the received signal  $\mathbf{x}(k)$  can be expressed as

$$\mathbf{x}(k) = \mathbf{A}(\theta)\mathbf{s}(k) + \mathbf{n}(k) = [x_1(k), x_2(k), \dots, x_{N_r}(k)]^T$$

$$(k = 1, 2, \dots, N_s), \quad (4.4)$$

where  $k$  denotes the time index for the sampled signals,  $N_r$  denotes the number of received antennas and  $\mathbf{A}(\theta) = [\mathbf{a}(\theta_1), \mathbf{a}(\theta_2), \dots, \mathbf{a}(\theta_G)]$  is a steering matrix composed of steering vectors that are expressed as

$$\mathbf{a}(\theta_g) = [e^{j\frac{2\pi}{\lambda}d_1 \sin \theta_g}, \dots, e^{j\frac{2\pi}{\lambda}d_u \sin \theta_g}, \dots, e^{j\frac{2\pi}{\lambda}d_{N_r} \sin \theta_g}]^T$$

$$(u = 1, 2, \dots, N_r), (g = 1, 2, \dots, G), \quad (4.5)$$

In addition,  $\mathbf{s}(k) = [s_1(k), s_2(k), \dots, s_G(k)]^T$  denotes the incident signal,  $\mathbf{n}(k) = [n_1(k), n_2(k), \dots, n_{N_r}(k)]^T$  denotes the zero-mean white Gaussian noise vectors whose noise variance is  $\sigma^2$ ,  $d_i$  denotes the distance between the  $i$ -th antenna element and the first antenna element, and  $[\cdot]^T$  denotes the transpose operator. Moreover, the probability density function of  $\mathbf{x}(k)$  can be expressed as

$$f(\mathbf{x}(k)) = \frac{1}{(2\pi\sigma^2)^{G/2}} e^{-\|\mathbf{x}(k) - \mathbf{A}(\theta)\mathbf{s}(k)\|^2/2\sigma^2}, \quad (4.6)$$

where  $\|\cdot\|$  denotes the Euclidean norm. To calculate the unknown parameters such as  $\sigma^2$  and  $\mathbf{s}(k)$ , the negative log-likelihood function  $l(\theta, \mathbf{s}(k), \sigma^2)$  is used. Since the measurements are independent, the negative log-likelihood function can be expressed as

$$l(\theta, \mathbf{s}(k), \sigma^2) = GN_s \log(2\pi\sigma^2) + \frac{1}{\sigma^2} \sum_{k=1}^{N_s} \|\mathbf{x}(k) - \mathbf{A}(\theta)\mathbf{s}(k)\|^2. \quad (4.7)$$

In Eq. (4.7),  $\hat{\sigma}^2$  and  $\hat{\mathbf{s}}(k)$ , which minimize the value of  $l(\theta, \mathbf{s}(k), \sigma^2)$  by partial differentiation, are obtained as follows [87].

$$\hat{\sigma}^2 = \frac{1}{G} \text{Tr}[(\mathbf{I} - \mathbf{A}(\theta)\mathbf{A}^\dagger(\theta))\hat{\mathbf{R}}], \quad (4.8)$$

$$\hat{\mathbf{s}}(k) = \mathbf{A}^\dagger(\theta)\mathbf{x}(k), \quad (4.9)$$

where  $\text{Tr}[\cdot]$  denotes the trace operator,  $\mathbf{I}$  denotes the identity matrix,  $\mathbf{A}^\dagger(\theta)$  denotes the pseudo-inverse of  $\mathbf{A}(\theta)$ , and  $\hat{\mathbf{R}}$  is the covariance matrix of  $\mathbf{x}(k)$ . Then, substituting

Eqs. (4.8) and (4.9) into Eq. (4.7) can be summarized as the following minimization problem,

$$\hat{\theta} = \underset{\theta}{\operatorname{argmin}} \operatorname{Tr}[(\mathbf{I} - \mathbf{A}(\theta)\mathbf{A}^\dagger(\theta))\hat{\mathbf{R}}]. \quad (4.10)$$

In (4.10),  $(\mathbf{I} - \mathbf{A}(\theta)\mathbf{A}^\dagger(\theta))$  corresponds to the orthogonal projector onto null space of  $\mathbf{A}^H(\theta)$ , where  $[\cdot]^H$  denotes the Hermitian operator. Furthermore, in this chapter, I define  $\operatorname{Tr}[(\mathbf{I} - \mathbf{A}(\theta)\mathbf{A}^\dagger(\theta))\hat{\mathbf{R}}]$  as an error function  $f_E(\theta)$ . The error function depends on  $\theta$  and has a small value when a target exists. Thus, if I find  $\hat{\theta}$  which minimizes the error function,  $\hat{\theta}$  is the DOA of the target.

### 4.3 Target detection in MIMO radar system

MIMO radar systems have an advantage in that the angular resolution is greatly improved because a large antenna aperture size can be obtained even with a small number of antenna elements. Figure 4.2 shows a MIMO radar system with two transmit antenna elements and four receiving antenna elements. In Fig. 4.2, two Tx and four Rx antennas are used in the MIMO radar system, but to obtain the same performance, one Tx and 8 Rx antennas have to be used in a single-input and multiple-output system [78], [80], [88]. Receiving signals at Rx1, 2, 3, 4 which are transmitted from Tx 2 are the same as receiving signals at the locations of virtual antenna elements which are transmitted from Tx 1. However, since the signals radiated from the two transmit antennas are superposed when they are received, it is necessary to distinguish the two different transmitted signals. If the two signals cannot be distinguished, the received signals are swapped and this results in a severe DOA estimation error. Figure 4.3 shows the structure of a true array and a false array. If the two transmitted signals are correctly distinguished, I can obtain the true array. However, if two transmitted signals are recognized reversely, the result which corresponds to the false array is obtained. When DOA estimation is performed using the false array, since each received signal is affected as if the phases are distorted, it is hard to estimate the accurate DOA

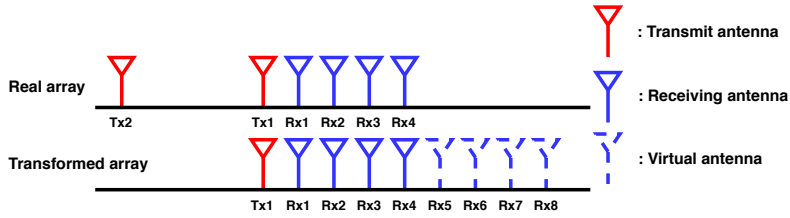


Figure 4.2: MIMO radar system with two transmit antenna elements and four received antenna elements

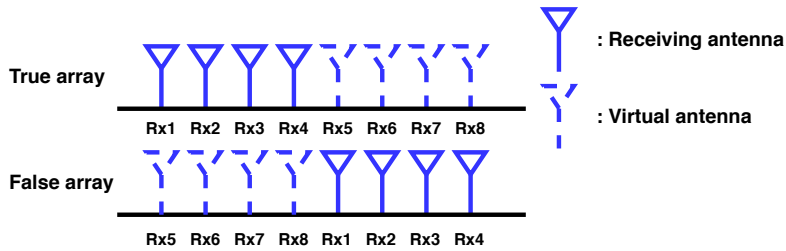


Figure 4.3: MIMO radar system with true array and false array

information.

Figure 4.4 shows the 2D-FFT results when the ranges and relative velocities of the targets are (10 m, 10 m/s), (10 m, -5 m/s). The radar parameters used in the simulation are presented in Table 4.1. There are actually two targets in this simulation, but since the targets are detected from each transmitted signal, four peaks are shown. Moreover, because of the circular characteristics of 2D-FFT, it is hard to determine the exact relative velocity of the target. Since the phase of the two different transmitted signals is shifted by  $\pi$ , the 2D-FFT result is shifted by a predetermined interval (i.e., the half of the maximum velocity detection range). Thus, I can know which two peaks represent the same target. However, it is hard to know which peak is matched with each transmitted signal. To find out which peaks are generated by the signals from which transmit antenna, I used the DML algorithm to find the true antenna array.

The transmitted signal matching method is as follows. First, using the result of 2D-FFT, I extract the peaks of the range-velocity (RV) spectrum. The number of peaks  $P$

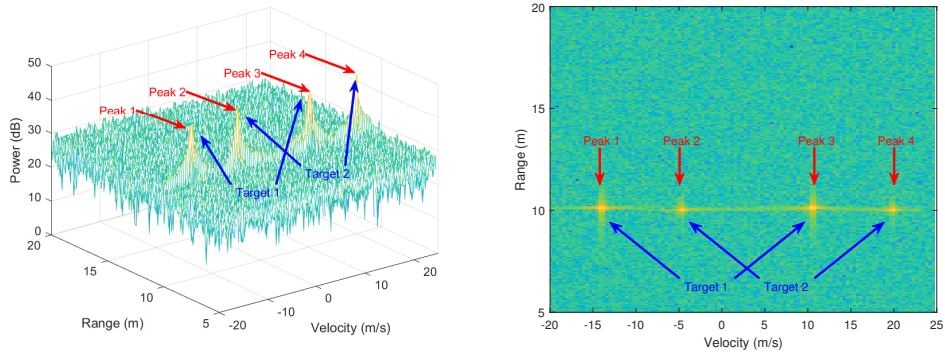


Figure 4.4: 2D-FFT result when two targets exist in same distance

Table 4.1: Values of radar parameters

Parameters	Value
$f_c$	76.5 GHz
$B$	800 MHz
$T_{sw}$	40 $\mu s$
$L$	128
$N_s$	512

in the RV spectrum is equal to the number of transmit antenna elements multiplied by the number of targets. Thus, the number of target  $G$  can be obtained by  $P/N_t$ . In Fig. 4.4, the peak 1 and the peak 3 represent the same target. One is the signal transmitted from Tx 1 and the other is the signal transmitted from Tx 2. If the signal obtained at peak 1 is  $\mathbf{x}_{(1)}$  and the signal obtained at peak 3 is  $\mathbf{x}_{(3)}$ , two array combinations  $\begin{bmatrix} \mathbf{x}_{(1)} \\ \mathbf{x}_{(3)} \end{bmatrix}$  and  $\begin{bmatrix} \mathbf{x}_{(3)} \\ \mathbf{x}_{(1)} \end{bmatrix}$  can be obtained. If the number of transmit antennas is  $N_t$ , the number of array combinations is  $N_t \cdot (N_t - 1) \cdots 2 \cdot 1 = N_t!$ . Figure 4.5 shows the 2D-FFT results when the ranges and relative velocities of two targets are different. The ranges and relative velocities of two targets are (15 m, 10 m/s) and (10 m, -5 m/s). Similarly in Fig. 4.4, peaks 1 and 3 represent the same target, and peaks 2 and 4 represent the same target.

Then, to distinguish the different transmitted signals, DML algorithm is applied to the extracted peaks which are obtained from each received signal. For example, in (4.10),  $\hat{\mathbf{R}}$  is substituted to  $\mathbf{R}_{(i,j)}$  and  $\mathbf{R}_{(j,i)}$ .

$$\mathbf{R}_{(i,j)} = E \left[ \begin{bmatrix} \mathbf{x}_{(i)} \\ \mathbf{x}_{(j)} \end{bmatrix} \begin{bmatrix} \mathbf{x}_{(i)} \\ \mathbf{x}_{(j)} \end{bmatrix}^T \right], \quad (4.11)$$

where  $E[\cdot]$  denotes the expectation operator and  $\mathbf{x}_{(i)}$  denotes the received signal extracted from  $i$ -th peak. Then, the error function is calculated using the covariance matrix obtained for each array combination. If the number of transmit antenna is  $N_t$ , the number of calculated error functions is  $N_t!$ . Thus, the error function of  $b$ -th array combination when the number of transmit antennas is  $N_t$  can be expressed as

$$f_{E_b}(\theta) = Tr[(\mathbf{I} - \tilde{\mathbf{A}}(\theta)\tilde{\mathbf{A}}^\dagger(\theta))\mathbf{R}_b] \\ (b = 1, 2, \cdots, N_t!), \quad (4.12)$$

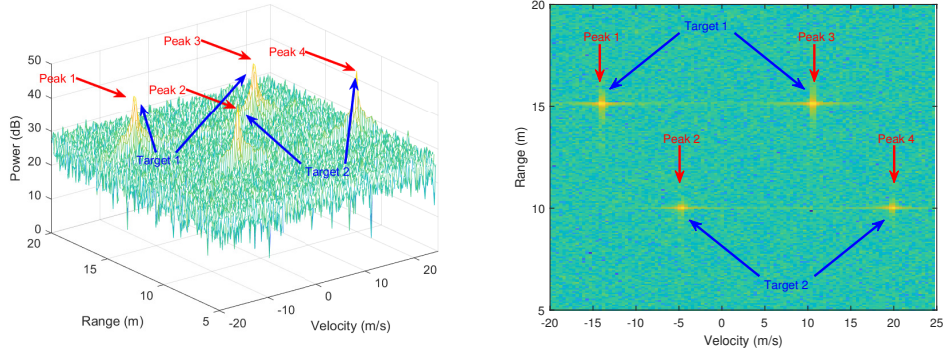


Figure 4.5: 2D-FFT result when two targets exist in different distance

where

$$\tilde{\mathbf{A}}(\theta) = \begin{bmatrix} e^{j\frac{2\pi}{\lambda}d_1\sin\theta_1} & \dots & e^{j\frac{2\pi}{\lambda}d_1\sin\theta_{N_D}} \\ \vdots & \ddots & \vdots \\ e^{j\frac{2\pi}{\lambda}d_{N_t \cdot N_r}\sin\theta_1} & \dots & e^{j\frac{2\pi}{\lambda}d_{N_t \cdot N_r}\sin\theta_{N_D}} \end{bmatrix}, \quad (4.13)$$

and  $R_b$  denotes the covariance matrix of  $b$ -th array combination. Furthermore, in (4.13),  $N_D$  denotes the number of angle samples which is determined by the target field of view and at which resolution the DOA is to be estimated. Then, the error function of the true array can be extracted by comparing the minimum values of error functions which is expressed as

$$\hat{b} = \arg \min_b (\min_{\theta} f_{E_b}(\theta)) \quad (b = 1, 2, \dots, N_t!). \quad (4.14)$$

Using the result in (4.14), I can find out which is the true array combination.

When the transmitted signal matching is correctly performed, the error function has the lowest value. When comparing the error function of each pair of arrays extracted from the RV spectrum, the array combination which has the smallest error function value is the true array. Thus, I can match the transmit signal with each corresponding peak extracted from the RV spectrum. Using this result, if the received signals from the true array are applied to DOA estimation algorithms such as the Capon

[89], multiple signal classification (MUSIC) [45] algorithm, I can estimate the exact DOAs of targets.

## 4.4 Simulation and experiment results

In this section, I verify the performance of the proposed method through simulations and actual experiments. More than two transmit antenna elements and four receiving antenna elements were used, and signal-to-noise ratio (SNR) was set to 10 dB. I estimated the DOAs of two different targets located at the same distance. To estimate the ranges and relative velocities of the targets, 2D-FFT was performed. Then, the peaks were extracted and DOA estimation algorithm was applied to the peaks. Figure 4.6 shows the DML estimation results. The number of targets is two and the DOAs of the two targets are  $-2^\circ$  and  $4^\circ$ . The ranges and relative velocities of the targets are shown in Fig. 4.4. In Fig. 4.6, the dotted lines denote the minimum values of the error functions which are proportional to the estimated noise variance. This value is the lowest when the antenna array combination is a true array. When the antenna array is incorrect, the result which is similar to phase distortion is shown. Because the phase is inaccurate, the minimum value of the error function is increased. Thus, the minimum value of the error function is smaller when using the true array than when using the false array.

Figure 4.7 shows the normalized pseudospectra of MUSIC and Capon. MUSIC and Capon are used to verify that the proposed method can be applied to various DOA estimation algorithms. The red and blue lines represent the normalized pseudospectra of the true and false array, respectively. The black dotted lines denote the DOAs of two targets. The DOAs of the targets are set to  $-2^\circ$  and  $4^\circ$ . DML is performed to find the correct array combination which corresponds to the true array in Fig. 4.6. However, if the transmit signal distinction is unsuccessful, the DOAs of the targets cannot be correctly estimated like the normalized pseudospectrum of the false array.

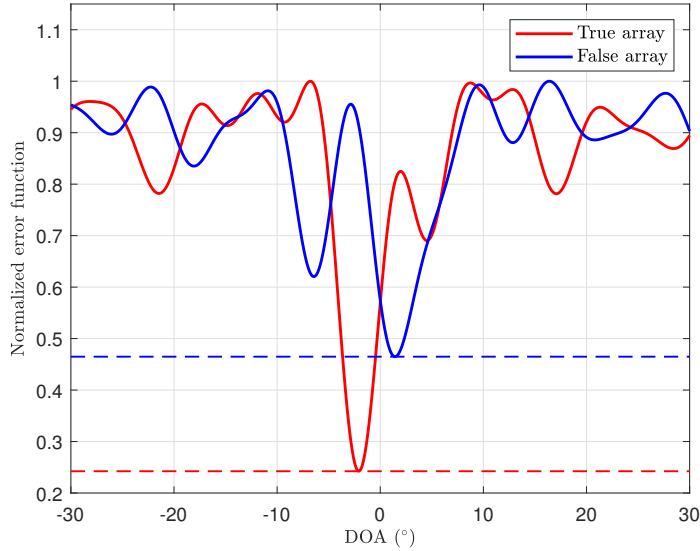
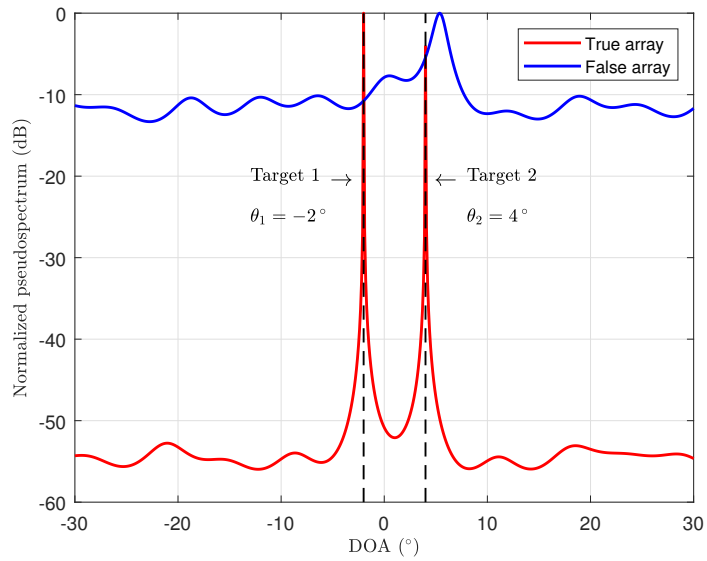


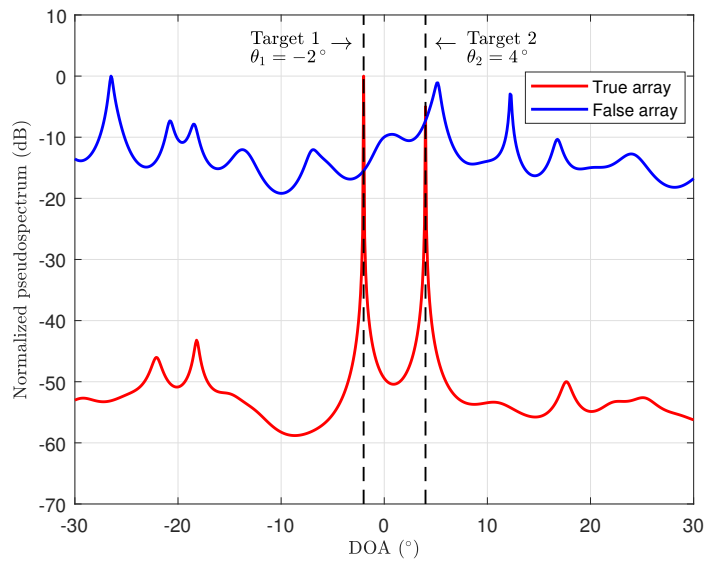
Figure 4.6: Normalized error function of true and false array

In addition to lowering the accuracy of the DOA estimation, the number of targets is also incorrectly estimated. On the other hand, when using the true array, the DOAs of the two targets are estimated correctly.

Furthermore, to verify that the proposed algorithm works well when there are more than three targets, simulations were performed with three targets in close proximity. Figure 4.8 shows the 2D-FFT result when the ranges, relative velocities, and DOAs of the targets are (10 m, -5 m/s,  $-3^\circ$ ), (15 m, 10 m/s,  $1^\circ$ ), (5 m, 5 m/s,  $6^\circ$ ), respectively. Since two transmit antennas are used, six peaks appear. Figure 4.9 shows the normalized error functions of true and false array. Even when three targets exist, the minimum value of the error function is smaller when using the true array. Since the MUSIC algorithm is a high resolution DOA estimation algorithm, it has excellent angle estimation and resolution performance. However, in Fig 4.10 (a), if the array combination is matched incorrectly, the DOAs of targets cannot be estimated properly. In Fig 4.10 (b), the Capon suffers from worse angle estimation performance than MUSIC when the array is not found correctly. As more adjacent targets are present, the importance



(a) MUSIC



(b) Capon

Figure 4.7: Normalized pseudospectra of true and false array (a) MUSIC (b) Capon

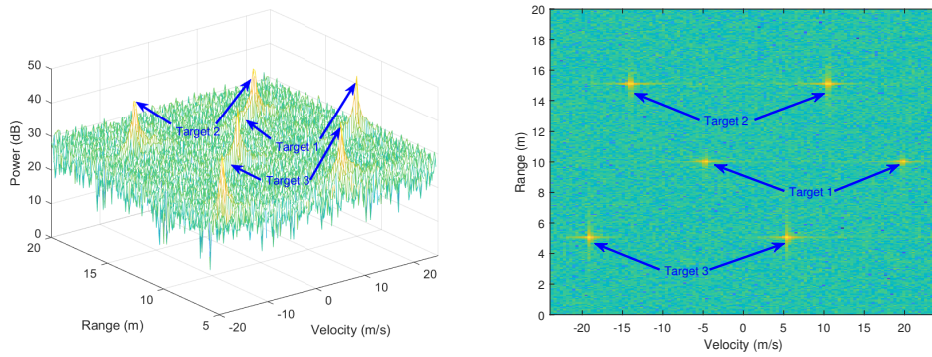


Figure 4.8: 2D-FFT results when three targets exist

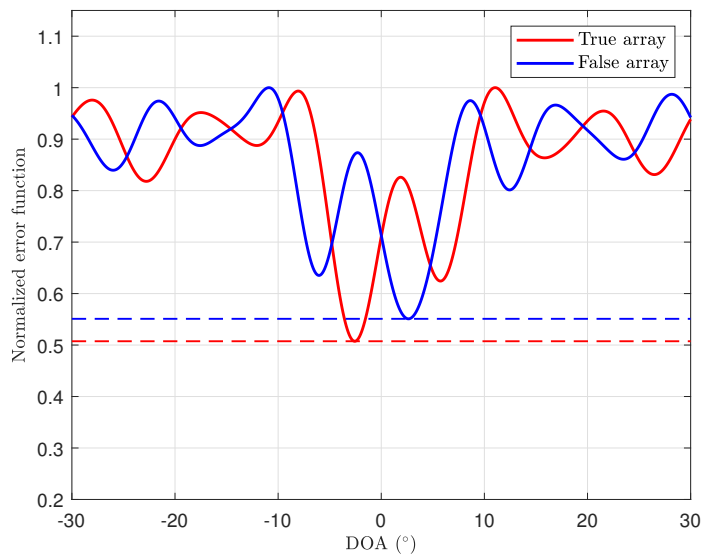
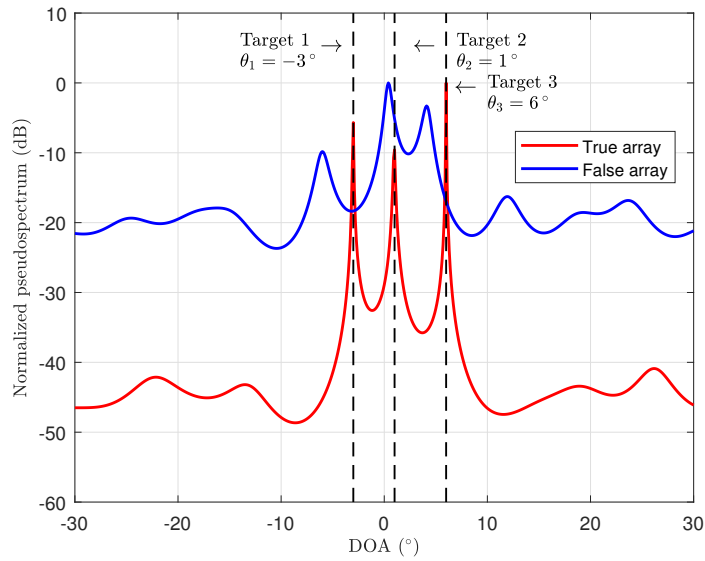
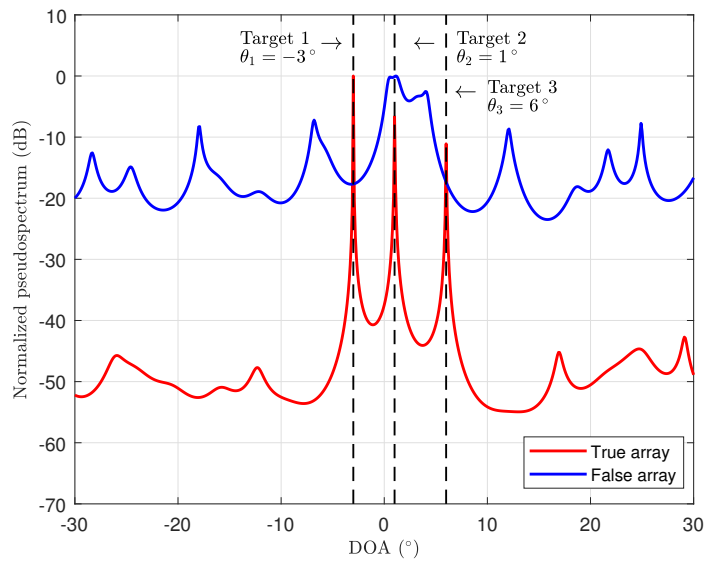


Figure 4.9: DML simulation results of true array and false array for three transmit antenna elements



(a) MUSIC



(b) Capon

Figure 4.10: Normalized pseudospectra of true array and false array for three targets

(a) MUSIC (b) Capon

of the proposed array matching method becomes apparent.

In addition, to verify that the proposed algorithm is applicable when more transmit antenna elements are used, simulations with three transmit antennas were performed. Figure 4.11 shows the possible array combinations of the MIMO radar system. Because three transmit antennas are used, the total number of array combination is  $3! = 6$ . Figure 4.12 shows the DML estimation results for the three transmit antenna elements. The number of targets is two and the DOAs of the two targets are  $-2^\circ$  and  $4^\circ$ . Similar to the two transmit antenna elements case, the true array has the lowest minimum value of the normalized error function. Table 4.2 shows the minimum values of the normalized error function according to the array combination. Compared to the false arrays, the minimum value of the normalized error function is the smallest in the case of the true array. Since the false array (1,2) and false array (3,4) are antenna arrays shifted with respect to each other, DOA estimation results are similar. The results of estimating the DOAs of the targets by applying the MUSIC and Capon algorithm to each array combination are shown in Fig. 4.13.

Next, in order to analyze the statistical performance of the proposed algorithm, I examined the change of resolution probability and root-mean-square error (RMSE) according to SNR. The resolution probability represents how many scans accurately estimate the number of targets among the total scans. The resolution probability was calculated as  $RP = \frac{N_o}{M} \times 100\%$ , where  $N_o$  is the number of scans that accurately estimate the number of targets and  $M$  denotes the number of simulation runs. In addition, the RMSE was calculated as

$$RMSE = \sqrt{\frac{\sum_{g=1}^G \sum_{m=1}^M (\theta_g - \hat{\theta}_g^{(m)})^2}{GM}} (^\circ), \quad (4.15)$$

where  $\theta_g$  and  $\hat{\theta}_g^{(m)}$  denote the actual DOA of the  $g$ -th target and the estimated DOA of the  $g$ -th target in the  $m$ -th ( $m = 1, 2, \dots, M$ ) simulation. Figure 4.14 shows the resolution probability according to SNR. In this simulation, SNR was varied from -20dB to 20dB at 1dB intervals, and simulations were carried out for each SNR 10,000

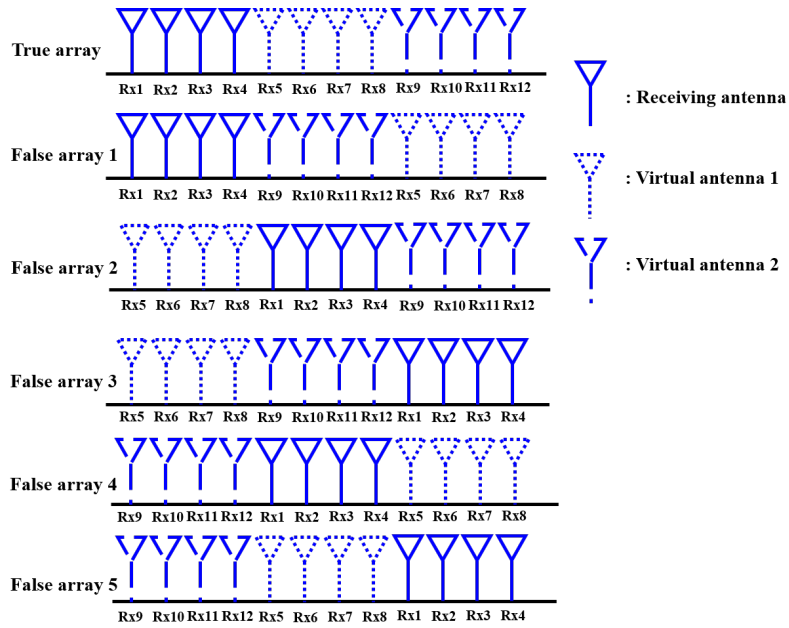


Figure 4.11: MIMO radar system with true array and false array with three transmit antennas

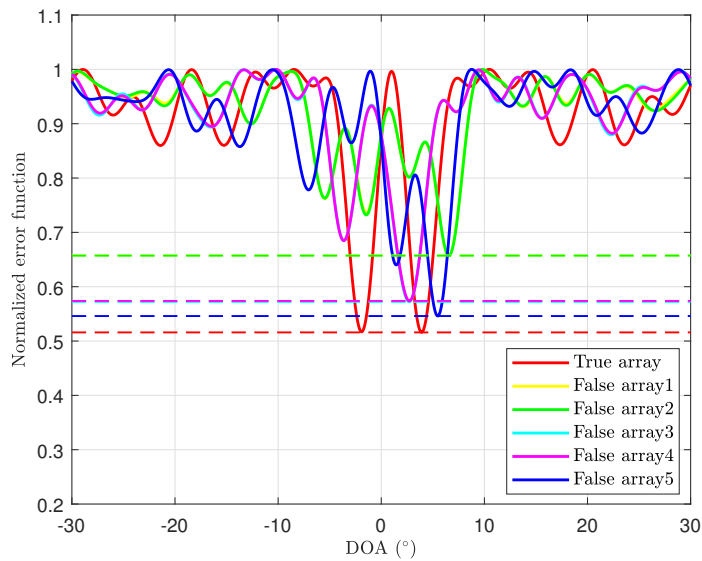


Figure 4.12: Normalized error function of true array and false array for three transmit antenna elements

Table 4.2: Minimum value of normalized error function according to the antenna array.

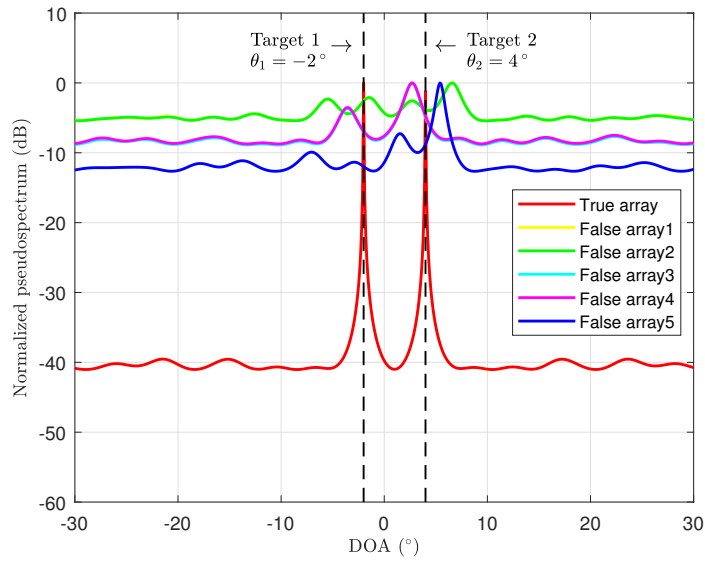
	Minimum value of normalized error function
True array	0.53832
False array 1	0.67704
False array 2	0.67738
False array 3	0.59902
False array 4	0.60445
False array 5	0.56506

Table 4.3: RMSE of true array and false array according to SNR

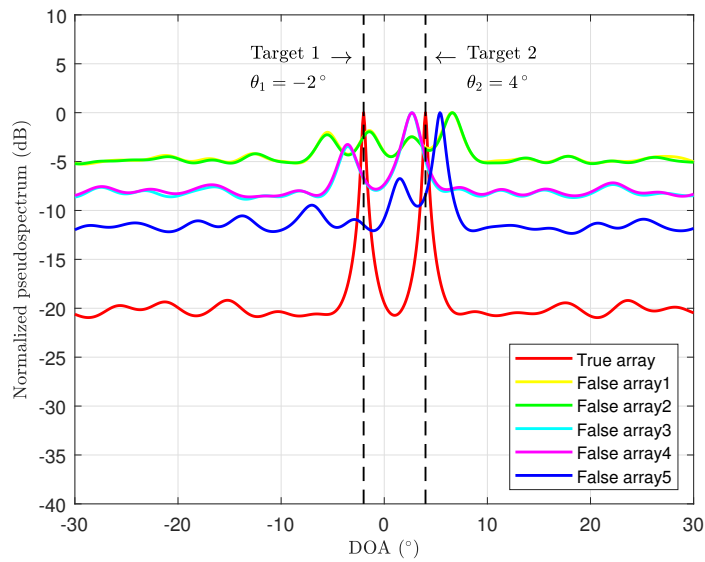
SNR/RMSE	True array	False array
-15 dB	0.5014	X
-5 dB	0.0832	3.1046
5 dB	0.0077	2.5231
15 dB	0	2.52

times. The number of targets is two and the angular spacing of the two targets are  $7^\circ$ . If array matching is done correctly, the number of targets is estimated accurately even at low SNR. In the case for false arrays, when the SNR is high, the number of targets is accurately detected, but the DOA estimation accuracy is low. The DOA estimation accuracy was analyzed by RMSE, which is shown in Table 4.3. I disregarded the RMSE for the case when the number of targets was incorrectly determined. If the true array is found correctly, a slight angle estimation error occurs when the SNR is low, but an angular error rarely occurs when the SNR is high. On the other hand, if array matching is unsuccessful, the DOA estimation error is quite large even at high SNR. Overall, using the proposed array matching method, the performance of DOA estimation is improved in terms of both resolution probability and RMSE.

Then, I verified the performance of the proposed method from experiments with



(a) MUSIC



(b) Capon

Figure 4.13: Normalized pseudospectra of true and false array for three transmit antenna (a) MUSIC (b) Capon

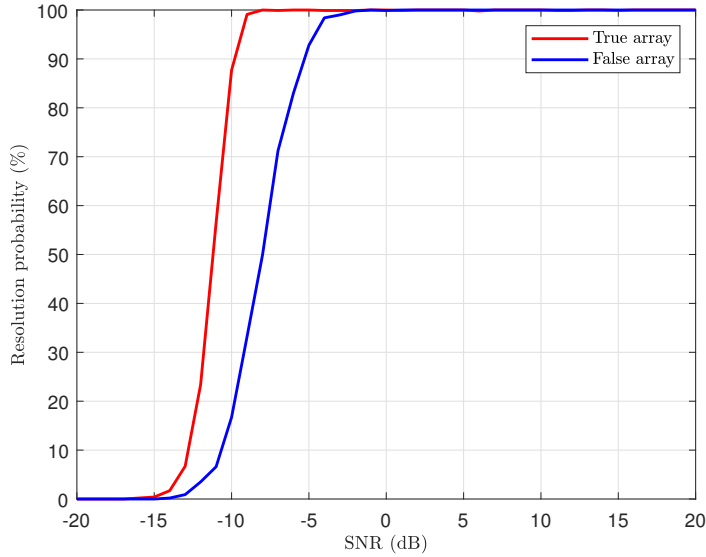


Figure 4.14: Resolution probability of true array and false array according to SNR

an actual automotive radar system. I conducted the experiments in a test field using a long-range radar manufactured by Hyundai Mobis (Republic of Korea). The number of transmit antennas is two and the number of receiving antennas is four. The maximum detection range of the radar system is 250 m and the field of view is from  $-10^\circ$  to  $10^\circ$ . In addition, the system transmits a 76.5 GHz fast-ramp frequency-modulated continuous wave radar signal with a bandwidth of 500 MHz and  $100 \mu s$  sweep time for up-chirp signals. In the experimental scenario, I placed two target vehicles and nothing else in the field of view of the radar system to mitigate the effects of other external factors and to analyze only the signals reflected from the two target vehicles. In addition, two targets were placed at the same distance from the radar-equipped vehicle to assume coherent received signals. Figure 4.15 shows the experimental environment. The DOAs of the two targets are  $-4^\circ$  and  $3^\circ$  respectively.

The target information was detected through 2D-FFT, and the DML algorithm was performed to find the true array. In accordance with the simulation results, if I execute the DML algorithm using experimental data, the minimum value of the error

function becomes smaller when the true array is used. In Fig. 4.16, the normalized error functions are shown. If the arrays are correctly matched, the minimum value of the error function is smaller than that of the false array case. Thus, I can distinguish between the true and false arrays. Using the DML results, I performed the MUSIC DOA estimation algorithm to find the DOAs of both targets correctly. In Fig. 4.17, the normalized MUSIC pseudospectra are presented. If the array matching fails, the two targets are not distinguished and estimating the number of targets accurately is impossible. However, if we find the true array by using the proposed algorithm, DOAs of the two targets are correctly estimated. The estimated DOAs are  $-3.9^\circ$  and  $2.7^\circ$ .



Figure 4.15: Experimental setup with two targets located in front of a radar-equipped vehicle

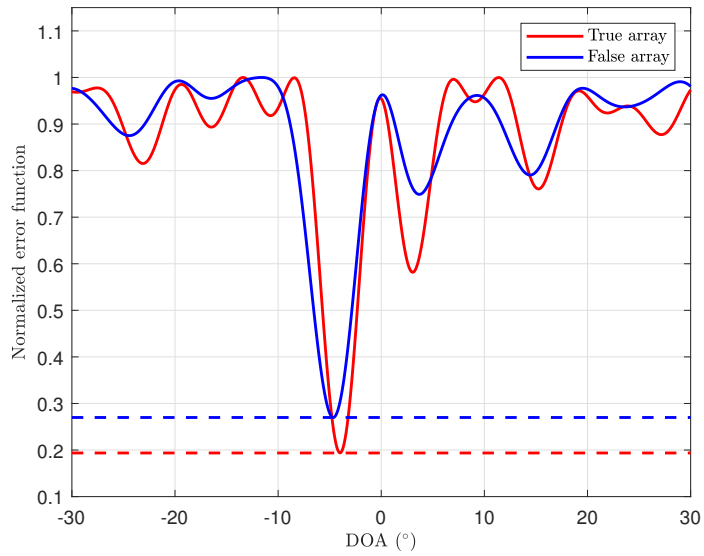


Figure 4.16: Normalized error function of true and false array in actual experiment

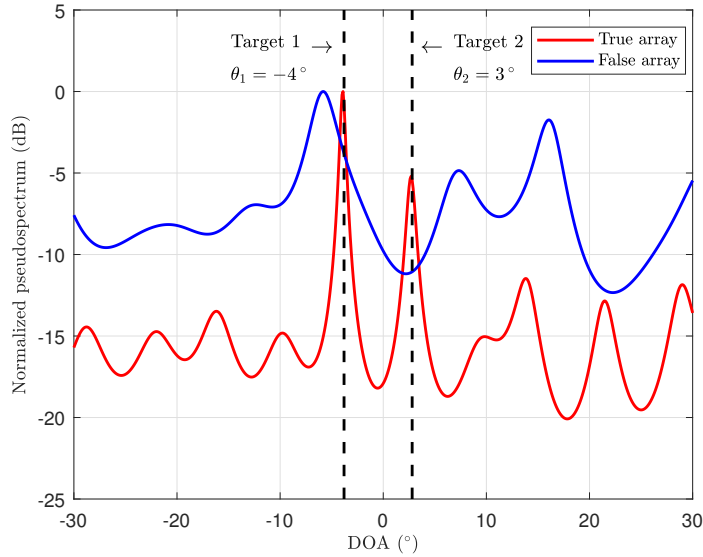


Figure 4.17: MUSIC experimental result of true and false array

## 4.5 Conclusion

In this chapter, I proposed a method to enhance the DOA estimation performance in a fast-ramp modulation MIMO radar system. Different transmitted signals were radiated using the space-time block code to distinguish the signals from each antenna. To solve the array mismatch problem that occurs when multiple transmit antennas are used, I applied the DML algorithm to the 2D-FFT peaks. Then, by comparing the minimum values of the normalized error functions, I found the true array combination. To verify the applicability in real-world environments, the proposed method was verified by simulations and experiments with an actual automotive radar system. As a result, I could distinguish different signals radiated from each of the transmit antennas, and the DOA estimation performance was enhanced in the fast-ramp MIMO radar system. The proposed method can thus be applied in various fields requiring distinctions between different transmitted signals.

## Chapter 5

### Conclusion

In this dissertation, I proposed various signal processing techniques for automotive radar. The research was conducted using a 77 GHz FMCW radar, which is mainly used in vehicles. I suggested various problems that could occur in a road environment during autonomous driving using radar sensors and proposed a method to solve these problems.

First, I proposed a method for recognizing and classifying various road environments. By recognizing and classifying the road environment in advance, the radar system can determine the performance degradation section in advance and apply an appropriate target detection algorithm. The road environments are classified by their different frequency magnitude response characteristics. A feedforward network structure suitable for road environment classification was then proposed to improve the road environment classification performance.

Next, I proposed a new extrapolation technique to solve the angular resolution problem that might occur in a complex road environment with many adjacent targets. Generally, the ranges and velocities of the targets could be used to separate adjacent targets. However, when the ranges and velocities are similar, a high resolution DOA estimation method is essential. Therefore, I generated a virtual received signal using the linearity in the ULA and achieved an improvement in angular resolution without

increasing the physical aperture size of the antenna.

Finally, I proposed a technique for distinguishing transmission signals in a MIMO radar. As a MIMO radar uses multiple transmission antennas, they must radiate transmission signals orthogonal to each other. In addition, different transmission signals can be distinguished from the receiving antenna to estimate the accurate positions of targets. In this dissertation, I improved the DOA estimation performance of a MIMO radar by distinguishing the transmission signals using the DML method.

# Bibliography

- [1] BIS Research: “Global automotive sensor market demand, supply and opportunities: estimation and forecast of (2015-2022),” August 2015.
- [2] M. I. Skolnik, *Introduction to radar systems*, McGraw-Hill, 2001.
- [3] W. D. Jones, “Keeping cars from crashing,” *IEEE Spectrum*, vol. 38, no. 9, pp. 40–45, September 2001.
- [4] H. Rohling, “A 77 GHz automotive radar system for AICC applications,” *International Conference on Microwaves and Radar (MIKON98)*, Krakow, Poland, 1998
- [5] H. Rohling and M. -M. Meinecke, “Waveform design principles for automotive radar systems,” *CIE International Conference on Radar Proceedings*, Beijing, China, October 2001, pp. 1–4.
- [6] M. Schneider, “Automotive radar - status and trends,” *IEEE German Microwave Conference*, Ulm, Germany, April 2005, pp. 351–354.
- [7] S. Lee and S. Kim, “Logarithmic-domain array interpolation for improved direction of arrival estimation in automotive radars,” *MDPI Sensors (Special Issue : Computational Intelligence in Remote Sensing)*, vol. 19, no. 10, pp. 1–21, May 2019.

- [8] H. Sim, S. Lee, S. Kang, and S. -C. Kim, "Enhanced DOA estimation using linearly predicted array expansion for automotive radar systems," *IEEE Access*, vol. 7, no. 1, pp. 47714–47727, April 2019.
- [9] S. Lee, Y. -J. Yoon, J. -E. Lee, and S. -C. Kim, "Human-vehicle classification using feature-based SVM in 77-GHz automotive FMCW radar," *IET Radar, Sonar & Navigation*, vol. 11, no. 10, pp. 1589–1596, October 2017.
- [10] S. Lee, Y. -J. Yoon, J. Yoon, H. Sim, and S. -C. Kim, "Periodic clutter suppression in iron road structures for automotive radar systems," *IET Radar, Sonar & Navigation*, vol. 12, no. 10, pp. 1146–1153, October 2018.
- [11] S. Lee, B. -h. Lee, J. -E. Lee, H. Sim, and S. -C. Kim, "Iron tunnel recognition using statistical characteristics of received signals in automotive radar systems," *IEEE International Radar Symposium*, Bonn, Germany, June 2018, pp. 1–8.
- [12] S. Lee, B. -h. Lee, J. -E. Lee, -E., and S. -C. Kim, "Statistical characteristic-based road structure recognition in automotive radar systems," *IEEE Transactions on Intelligent Transportation Systems*, vol. 20, no. 7, pp. 2418–2429, September 2019.
- [13] J. Yoon, S. Lee, S. Lim, and S. -C. Kim, "High-density clutter recognition and suppression for automotive radar systems," *IEEE Access*, vol. 7, no. 1, pp. 58368–58380, May 2019.
- [14] H. Sim, H., Lee, S., Lee, B.-h., and S. -C. Kim, "Road structure classification through artificial neural network for automotive radar systems," *IET Radar, Sonar & Navigation*, vol. 13, no. 6, pp. 1010–1017, June 2019.
- [15] A. G. Stove, "Linear FMCW radar techniques," *IEE Proc F, Radar Signal Process*, vol. 139, no. 5, pp. 343–350, October 1992.

- [16] B. R. Mahafza, *Radar Systems Analysis and Design Using MATLAB*, Chapman and Hall/CRC, 2000.
- [17] V. Winkler, "Range doppler detection for automotive FMCW radars," *IEEE European Radar Conference*, Munich, Germany, October 2007, pp. 166–169.
- [18] S. Lutz, D. Ellenrieder, T. Walter, and R. Weigel, "On fast chirp modulations and compressed sensing for automotive radar applications," *IEEE International Radar Symposium*, Gdansk, Poland, June 2014, pp. 1–6.
- [19] L. L. Nagy, "Electromagnetic reflectivity characteristics of road surfaces," *IEEE Transactions on Vehicular Technology*, vol. 23, no. 4, pp. 117–124, November 1974.
- [20] R. Schneider, D. Didascalou, and W. Wiesbeck, "Impact of road surfaces on millimeter-wave propagation," *IEEE Transactions on Vehicular Technology*, vol. 49, no. 4, pp. 1314–1320, July 2000.
- [21] P. H. Pathak, W. D. Burnside, and R. J. Marhefka, "A uniform GTD analysis of the diffraction of electromagnetic waves by a smooth convex surface," *IEEE Transactions on Antenna Propagation*, vol. 28, no. 5, pp. 631–642, September 1980.
- [22] I. Matsunami and A. Kajiwara, "Clutter suppression scheme for vehicle radar," *IEEE Radio and Wireless Symposium*, LA, USA, January 2010, pp. 320–323.
- [23] Y. -Z. Ma, C. Cui, B. -S. Kim, J. -M. Joo, S. H. Jeon, and S. Nam, "Road clutter spectrum of BSD FMCW automotive radar," *IEEE European Radar Conference*, Paris, France, September 2015, pp. 109–112.
- [24] J. -E. Lee, H. -S. Lim, S. -H. Jeong, S. -C. Kim, and H. -C. Shin, "Enhanced iron-tunnel recognition for automotive radars," *IEEE Transactions on Vehicular Technology*, vol. 65, no. 6, pp. 4412–4418, January 2016.

- [25] H. -B. Lee, J. -E. Lee, H. -S. Lim, S. -H. Jeong, and S. -C. Kim, "Clutter suppression method of iron tunnel using cepstral analysis for automotive radars," *IEICE Transactions on Communications*, vol. E100-B, no. 2, pp. 400–406, February 2017.
- [26] J. -E. Lee, H. -S. Lim, S. -H. Jeong, H. -C. Shin, S. -W. Lee, and S. -C. Kim, "Harmonic clutter recognition and suppression for automotive radar sensors," *International Journal of Distributed Sensor Networks*, vol. 13, no. 9, pp. 1–11, September 2017.
- [27] K. Takagi, K. Morikawa, T. Ogawa, and M. Saburi, "Road environment recognition using on-vehicle LIDAR", *IEEE Intelligent Vehicle Symposium*, Tokyo, Japan, June 2006, pp. 120–125.
- [28] A. Broggi, P. Cerri, P. Medici, P. P. Porta, and G. Ghisio, "Real time road signs recognition," *IEEE Intelligent Vehicle Symposium*, Istanbul, Turkey, June 2007, pp. 981–986.
- [29] L. Zhou and Z. Deng, "LIDAR and vision-based real-time traffic sign detection and recognition algorithm for intelligent vehicle," *IEEE International Conference on Intelligent Transportation Systems*, Qingdao, China, October 2014, pp. 578–583.
- [30] H. Guan, J. Li, Y. Yu, Z. Ji, and C. Wang, "Using mobile LiDAR data for rapidly updating road markings," *IEEE Transactions on Intelligent Transportation Systems*, vol. 16, no. 5, pp. 2457–2466, October 2015.
- [31] A. Y. Hata, and D. F. Wolf, "Feature detection for vehicle localization in urban environments using a multilayer LIDAR," *IEEE Transactions on Intelligent Transportation Systems*, vol. 17, no. 2, pp. 420–429, February 2016.
- [32] G. Minkler and J. Minkler, *CFAR: the principles of automatic radar detection in clutter*, Magellan, 1990.

- [33] L. Kong, B. Wang, G. Cui, W. Yi, and X. Yang, "Performance prediction of OS-CFAR for generalized Swerling-Chi fluctuating targets," *IEEE Transactions on Aerospace and Electronic Systems*, vol. 52, no. 1, pp. 492–500, February 2016.
- [34] Y. LeCun, *et al.*, "Handwritten digit recognition with a back-propagation network," *Advances in Neural Information Processing Systems*, Denver, CO, USA, November 1990, pp. 396–404.
- [35] A. Krizhevsky, I. Sutskever, and G. Hinton, "ImageNet classification with deep convolutional neural networks," *Advances in Neural Information Processing Systems*, Lake Tahoe, NV, USA, December 2012, pp. 1106–1114.
- [36] A. Graves, A. -R. Mohamed, and G. Hinton, "Speech recognition with deep recurrent neural networks," *IEEE International Conference on Acoustics, Speech and Signal Processing*, Vancouver, Canada, May 2013, pp. 6645–6649.
- [37] K. He and S. Ren "Convolutional neural networks at constrained time cost," *IEEE Conference on Computer Vision and Pattern Recognition*, Boston, MA, USA, June 2015, pp. 3791-3799.
- [38] Y. Chauvin and D. E. Rumelhart, *Back propagation : theory, architectures, and applications*, Lawrence Erlbaum Associates, 1995.
- [39] M. Cheriet, *Character Recognition Systems*, A John Wiley and Sons, 2007.
- [40] O. N. A. Al-Allaf, S. A. Abdalkader, and A. A. Tamimi, "Pattern recognition neural network for improving the performance of iris recognition system," *Journal of Scientific and Engineering Research*, vol. 4, no. 6, June 2013, pp. 661–667.
- [41] M. Ahmed, M. T. Imtiaz, and R. Khan, "Movie recommendation system using clustering and pattern recognition network," *IEEE Computing and Communication Workshop and Conference*, Las Vegas, NV, USA, January 2018, pp. 143–147.

- [42] D. E. Rumelhart and J. L. McClelland, *Parallel distributed processing : explorations in the microstructures of cognition*, MIT Press, 1986.
- [43] B. Karlik and A. V. Olgac, "Performance analysis of various activation functions in generalized MLP architectures of neural networks," *International Journal of Artificial Intelligence and Expert Systems*, vol. 1, no. 4, pp. 111–122, February 2011.
- [44] M. S. Bartlett, "Periodogram analysis and continuous spectra," *Biometrika*, vol. 37, no. 1/2, pp. 1–16, June 1950.
- [45] R. O. Schmidt, "Multiple emitter location and signal parameter estimation," *IEEE Transactions on Antennas and Propagation*, vol. 34, no. 3, pp. 276–280, March 1986.
- [46] R. T. Williams, S. Prasad, A. K. Mahalanabis, and L. H. Sibul, "An improved spatial smoothing technique for bearing estimation in a multipath environment," *IEEE Transactions on Acoustics Speech, and Signal Processing*, vol. 36, no. 4, pp. 425–432, April 1988.
- [47] M. Wax and J. Sheinvald, "Direction finding of coherent signals via spatial smoothing for uniform circular arrays," *IEEE Transactions on Antennas Propagation*, vol. 42, no. 5, pp. 613–620, May 1994.
- [48] C. -L. Liu and P. Vaidyanathan, "Remarks on the spatial smoothing step in coarray MUSIC," *IEEE Signal Processing Letters*, vol. 22, no. 9, pp. 1438–1442, September 2015.
- [49] M. A. Richards, *Fundamentals of Radar Signal Processing*, McGraw-Hill, 2005.
- [50] S. J. Orfanidis, "Electromagnetic Waves and Antennas," [Online] Available at: <http://www.ece.rutgers.edu/orfanidi/ewa>

- [51] B. Friedlander, "Direction finding using an interpolated array," IEEE International Conference on Acoustics, Speech, and Signal Processing, Albuquerque, NM, USA, April 1990, pp. 2951–2954.
- [52] A. J. Weiss and M. Gavish, "Direction finding using ESPRIT with interpolated arrays," IEEE Transactions on Signal Processing, vol. 39, no. 6, pp. 1473–1478, January 1991.
- [53] B. Friedlander, "The root-MUSIC algorithm for direction finding with interpolated arrays," ELSEVIER Signal Processing, vol. 30, no. 1, pp. 15–29, January 1993.
- [54] S. Kang, S. Lee, J. -E. Lee, and S. -C. Kim, "Improving the performance of DOA estimation using virtual antenna in automotive radar," *IEICE Transactions on Communications*, vol. E100-B, no. 5, pp. 771–778, May 2017.
- [55] T. E. Tuncer, T. K. Yasar, and B. Friedlander, "Direction of arrival estimation for nonuniform linear arrays by using array interpolation," *Radio Science*, vol. 42, no. 4, pp. 1–11, Aug 2007.
- [56] K. Kim, T. K. Sarkar, and M. S. Palma, "Adaptive processing using a single snapshot for a nonuniformly spaced array in the presence of mutual coupling and near-field scatterers," *IEEE Transactions on Antennas and Propagation*, vol. 50, no. 5, pp. 582–590, May 2002.
- [57] D.N. Swingler, R.S. Walker, and G.B. Lewis, "Linear prediction for aperture extrapolation in line array beamforming," *IEEE International Conference Acoustics, Speech, and Signal Processing*, Tokyo, Japan, April 1986, pp. 2519–2522.
- [58] D.N. Swingler and R.S. Walker, "Line-array beamforming using linear prediction for aperture interpolation and extrapolation," *IEEE Transactions on Acoustics, Speech, and Signal Processing*, vol. 37, no. 1, pp. 16–30, January 1989.

- [59] A. T. Moffet, "Minimum-redundancy linear arrays," *IEEE Transactions on Antennas and Propagation*, vol. 16, no. 2, pp. 172–175, March 1968.
- [60] M. Ishiguro, "Minimum redundancy linear arrays for a large number of antennas," *Radio Science*, vol. 15, no. 6, pp. 1163–1170, Nov.-Dec 1980.
- [61] P. Pal and P. P. Vaidyanathan, "Nested arrays in two dimensions, part II: application in two dimensional array processing," *IEEE Transactions on Signal Processing*, vol. 60, no. 9, pp. 4706–4718, September 2012.
- [62] P. Pal and P. P. Vaidyanathan, "Nested arrays: a novel approach to array processing with enhanced degrees of freedom," *IEEE Transactions on Signal Processing*, vol. 58, no. 8, pp. 4167–4181, August 2010.
- [63] P. P. Vaidyanathan and P. Pal, "Sparse sensing with co-prime samplers and arrays," *IEEE Transactions on Signal Processing*, vol. 59, no. 2, pp. 573–586, February 2011.
- [64] Z. Tan, Y. C. Eldar, and A. Nehorai, "Direction of arrival estimation using co-prime arrays: a super resolution viewpoint," *IEEE Transactions on Signal Processing*, vol. 62, no. 21, pp. 5565–5576, November 2014.
- [65] Z. Ye and X. Xu, "DOA Estimation by Exploiting the Symmetric Configuration of Uniform Linear array," *IEEE Transactions on Antennas Propagation*, vol. 55, no. 12, pp. 3716–3720, December 2007.
- [66] Z. Ye, J. Dai, X. Xu, and X. Wu, "DOA Estimation for uniform Linear array with mutual coupling," *IEEE Transactions on Aerospace and Electronic Systems*, vol. 45, no. 1, pp. 280–288, January 2009.
- [67] H. Krim and M. Viberg, "Two decades of array signal processing research: the parametric approach," *IEEE Signal Processing Magazine*, vol. 13, no. 4, pp. 67–94, July 1996.

- [68] G. H. Golub, "Numerical methods for solving linear least squares problems," *Numerische Mathematik*, vol. 7, no. 3, pp. 206–216, June 1965.
- [69] S. Lee, Y.-J. Yoon, J.-E. Lee, H. Sim, and S.-C. Kim, "Two-stage DOA estimation method for low SNR signals in automotive radars," *IET Radar, Sonar & Navigation*, vol. 11, no. 11, pp. 1613–1619, November 2017.
- [70] A. Ossowska, *Highly resolved synthetic aperture radar with beam steering*, KIT scientific, 2015.
- [71] S. Haykin, *Adaptive Filter Theory*, Prentice-Hall, 1991.
- [72] H. Rohling and C. Moller, "Radar waveform for automotive radar systems and applications," *IEEE Radar Conference*, Rome, Italy, May 2008, pp. 1–4.
- [73] E. Fishler, A. Haimovich, A., R. Blum, D. Chizhik, L. Cimini, and R. Valenzuela, "MIMO radar: An idea whose time has come," *IEEE Radar Conference*, Philadelphia, PA, USA, April 2004, pp. 71–78.
- [74] J. Li and P. Stoica, "MIMO Radar with colocated antennas," *IEEE Signal Processing Magazine*, vol. 24, no. 5, pp. 106–114, October 2007.
- [75] A. M. Haimovich, R. S. Blum, and L. J. Cimini, "MIMO Radar with widely separated antennas," *IEEE Signal Processing Magazine*, vol. 25, no. 1, pp. 116–129, December 2007.
- [76] B. J. Donnet and I. D. Longstaff, "MIMO radar techniques and opportunities," *IEEE European Radar Conference*, Manchester, UK, September 2006, pp. 112–115.
- [77] J. Li and P. Stoica, "MIMO radar-diversity means superiority," *Proc. 14th Annu. Workshop Adaptive Sensor Array Processing*, MIT Lincoln Laboratory, Lexington, MA, USA, June 2006.

- [78] J. Li, P. Stoica, L. Xu, and W. Roberts, "On parameter identifiability of MIMO radar," *IEEE Signal Processing Letter*, vol. 14, no. 12, pp. 968–971, December 2007.
- [79] J. Ender and J. Klare, "System architectures and algorithms for radar imaging by MIMO-SAR," IEEE Radar Conference, Pasadena, CA, USA, May 2009, pp. 1–6.
- [80] J. Klare, O. Saalman, H. Wilden, and A. R. Brenner, "First experimental results with the imaging MIMO radar MIRA-CLE X," 2010 8th European Conference on Synthetic Aperture Radar (EUSAR), Aachen, Germany, June 2010, pp. 1–4.
- [81] S. Lutz, K. Baur, and T. Walter, "77GHz lens-based multistatic MIMO radar with colocated antennas for automotive applications," *IEEE Microwave Symposium Dig.*, Montreal, QC, Canada, June 2012, pp. 1–3.
- [82] J. J. M. De Wit, W. L. van Rossum, and A. J. de Jong, "Orthogonal waveforms for FMCW MIMO radar," IEEE Radar Conference, Kansas City, MO, USA, May 2011, pp. 686–691.
- [83] F. Gini, A. De Maio, and L. Patton, *Waveform design and diversity for advanced radar systems*, (Institution of Engineering and Technology, New York, NY, USA, 2012)
- [84] Tarokh, V., Seshachi, N., and Calderbank, A.R.: "Space-time codes for high data rate wireless communications: performance analysis and code construction," *IEEE Transactions on Information Theory*, vol. 44, no. 2, pp. 744–765, March 1998.
- [85] S. M. Alamouti, "A simple transmit diversity technique for wireless communications," *IEEE Journal on Selected Areas in Communications*, vol. 16, no. 8, pp. 1451–1458, October 1998.

- [86] H. Sun, F. Brigui, and M. Lesturgie, "Analysis and comparison of MIMO radar waveforms," *International Radar Conference*, Lille, France, October 2014, pp. 1–6.
- [87] J. F. Bohme, "Estimation of source parameters by maximum likelihood and non-linear regression," *IEEE International Conference on Acoustics, Speech, and Processing*, San Diego, CA, USA, March 1984, pp. 7.3.1-7.3.4.
- [88] D. W. Bliss and K. W. Forsythe, "Multiple-input multiple-output (MIMO) radar and imaging: Degrees of freedom and resolution," *37th Asilomar Conference on Signals, Systems & Computation*, Pacific Grove, CA, USA, Nov 2003, pp. 54–59.
- [89] J. Capon, "High-resolution frequency-wavenumber spectrum analysis," *IEEE*, vol. 57, no. 8, pp. 1408–1418, August 1969.

# 초 록

최근 들어, 자율 주행 자동차와 관련된 관심이 높아지면서 자율 주행에 사용되는 센서들과 관련된 연구가 활발히 진행되고 있다. 자율 주행에 사용되는 센서에는 카메라, 라이다, 레이더, 초음파 등이 있는데, 그 중에서 레이더는 최대 탐지 가능 거리가 길고, 빛이 없는 상황이나 비가 오는 상황 등 열악한 환경에 강인한 특성을 가지고 있어서 자율주행에 필수적이다. 레이더는 다양한 용도로 사용이 가능한데, 주로 적응형 순항 제어와 자동 긴급 제동에 사용된다. 레이더는 원하는 타겟까지의 거리, 상대속도, 각도 등을 탐지할 수 있고, 타겟의 종류, 크기 등에 대해서도 탐지가 가능하다.

본 학위 논문에서는 도로 환경을 분류할 수 있는 인공 신경망 구조를 제안하였다. 자율주행을 하다 보면 다양한 도로 환경을 마주하게 되는데, 도로 환경에 따라 그에 맞는 타겟 검출 알고리즘을 적용할 필요가 있다. 예를 들어, 여러 개의 철제 구조물로 이루어진 철제 터널의 경우에는 반사 신호가 아주 강해서 타겟이 묻히게 되는 현상이 발생하게 된다. 따라서, 원하는 타겟을 검출하기 위해서는 클러터 제거 알고리즘을 적용하는 것이 필요하다. 본 논문에서는 각각의 도로 환경에 적합한 알고리즘을 적용하기 위한 사전 작업으로 딥러닝 기법을 이용하여 도로 환경을 분류하고, 도로 환경을 멀리서도 미리 인식하는 인공 신경망의 구조 제안하였다. 결과적으로, 도로 환경 분류 정확도를 약 14%p 정도 향상시켰다.

또한, 차량용 레이더를 이용하여 각도 분해능을 향상 시킬 수 있는 기법을 제안하였다. 타겟의 위치 정보를 알기 위해서는 거리, 속도 정보 이외에도 각도 정보가 필수적이다. 하지만, 서로 다른 두 타겟이 가까이에 위치하게 되면, 각도 분해능의

한계로 인해 두 타깃이 한 타깃으로 나타나는 현상이 발생하게 된다. 이는 안테나 개구면의 크기를 늘려서 해결이 가능하지만 개구면의 크기를 늘리게 되면 시야각이 줄어들고, 물리적인 공간도 많이 차지하게 되는 단점이 있다. 이를 해결하기 위해 본 논문에서는 선형 예측 안테나 외삽 방식을 이용하여 가상의 수신 신호를 생성하는 방식을 제안하였다. 생성된 가상의 수신 신호와 실제 신호를 도래각 추정 알고리즘에 적용하여 작은 안테나 개구면의 크기를 사용하면서도 각도 분해능은 향상시키는 방법을 제안하였다. 결과적으로, 제안한 기법을 이용하여 각도 분해능을 약 3° 가량 향상시켰다.

마지막으로, 레이더에서의 송신 신호 분류 기법을 제안하여 타깃의 위치 추정 성능을 향상시켰다. 여러 개의 송신 안테나를 사용하게 되면 적은 개수의 안테나를 이용하여 타깃을 효율적으로 검출할 수 있다. 하지만, 각각의 송신 안테나로부터 방사된 신호를 구분하지 못하게 되면, 각도 추정 성능에 열화가 발생한다. 이러한 문제를 해결하기 위해 최대 우도 추정 기법을 이용하여 송신 신호를 분류하는 기법을 제안하였다. 결과적으로, 최대로 탐지 가능한 속도 범위를 2배로 증가시켰다. 또한, 송신 신호를 구분하는 기법을 이용하여 각도의 평균 제곱은 오차를 3° 정도 향상시켰다.

**주요어:** MIMO 레이더, 가상 안테나, 도래각, 도로 환경 분류, 도로 환경 인식, 딥러닝, 차량용 레이더

**학번:** 2014-21629